Ore Geology Reviews 150 (2022) 105184

Contents lists available at ScienceDirect

Ore Geology Reviews

journal homepage: www.elsevier.com/locate/oregeorev

Effective delineation of rare metal-bearing granites from remote sensing data using machine learning methods: A case study from the Umm Naggat Area, Central Eastern Desert, Egypt

Mohamed A. Abdelkader [a,b], Yasushi Watanabe [a], Ali Shebl [c,d,*], Hanna A. El-Dokouny [b], Maher Dawoud [b], Árpád Csámer [c]

[a] Department of Earth Resource Science, Akita University, Japan
[b] Department of Geology, Faculty of Science, Menoufia University, Egypt
[c] Department of Mineralogy and Geology, University of Debrecen, Hungary
[d] Department of Geology, Faculty of Science, Tanta University, Egypt

ARTICLE INFO

Keywords:
Sentinel-2
ASTER
Support Vector Machine
Albitized granite
Integrated image processing techniques
Rare-metal exploration
Central Eastern Desert
Egypt

ABSTRACT

Albitized granite (ABG) is considered as one of the most significant hosts of rare metals (RMs). Consequently, adequate recognition of ABG through proper lithological discrimination highly increases the targeting of rare metal resources. In order to delineate outcrops of ABG from satellite data, our study integrates eight image enhancement techniques, including optimum index factor, false color composites, band rationing, relative band depth, independent component analysis, principal component analysis, decorrelation stretch, minimum noise fraction transform, and spectral indices ratios, for the interpretation of ASTER and Sentinel-2 (S2) datasets. This integrated approach allows the effective discrimination of AGB outcrops in the Umm Naggat area, Central Eastern Desert, Egypt. The interpretation maps derived from these integrated image processing techniques were systematically verified in the field and formed the base for the feature selection process (i.e., training and testing data delineation) of different lithologies supported by the support vector machine algorithm (SVM). In order to produce a high-quality lithological interpretation map, SVM was applied to Sentinel-2, ASTER, and combined ASTER-S2 datasets. The fused ASTER-S2 classification properly delineates ABG, as verified by our field investigations and confirmed by previous geological maps. Furthermore, comprehensive structural analysis (lineaments extraction and their density map) and hydrothermal alteration detection were performed to check the spatial association between the distribution of ABG, higher density zones, and highly altered areas, that in turn, could shed light on new potentially mineralized zones and proposed exploration targets. Our study reveals new ABG occurrences mainly situated in the southern and southwestern parts of the study area, and it confirms the location of known mineralized zones in the northern part of the Umm Naggat region. The distribution of ABG and its spatial correlation with alteration and high structural density zones suggest that rare-metal mineralization is mostly structurally controlled (NW, NNW, NNE, and N-S), demonstrating the higher possibility of metasomatic enrichment of rare-metals within the study area. Our study provides an updated geological map of the study area based on the SVM-supported interpretation of ASTER-S2 data. Importantly, the results reveal a high exploration potential for rare-metal mineralization at Umm Naggat and defining new anomalies for follow-up work by geochemical soil surveys.

1. Introduction

Continental shields, such as the Arabian-Nubian Shield (ANS) represent a significant source of various mineral deposits (Ahmed, 2022, Hamimi et al., 2020a). The ANS is exposed on both sides of the Red Sea, forming one of the most extensive surface outcrops of the Precambrian continental crust (Abd El-Wahed et al., 2019, Ahmed, 2022). The ANS granitic rocks host various mineral deposit types, such as rare metals, which explains why exploration attempts for ore resources have resulted in numerous discoveries in ANS countries.

* Corresponding author.
E-mail address: ali.shebl@science.tanta.edu.eg (A. Shebl).

https://doi.org/10.1016/j.oregeorev.2022.105184
Received 10 September 2022; Received in revised form 27 October 2022; Accepted 30 October 2022
Available online 1 November 2022

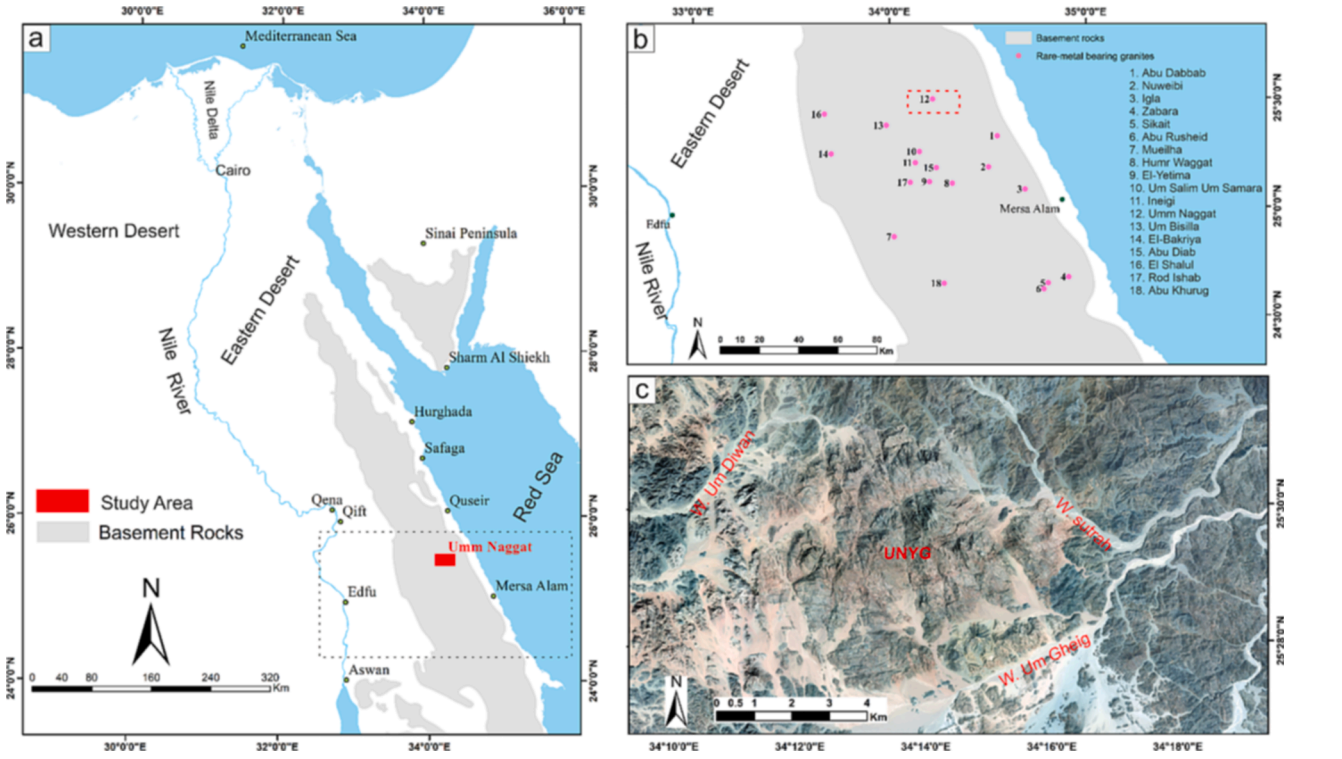

Fig. 1. (a) Basement rocks occurrences in the Eastern Desert of Egypt showing the location of the Umm Naggat area. (b) Distribution of some rare metals-bearing granites around the study area (modified after Zoheir et al. (2020)). (c) Google Earth image of the study area showing Umm Naggat Younger granite (UNYG) pluton and main surrounding Wadis.

Granitic rocks comprise around 50 % of the Neoproterozoic tract of the northern ANS, including northwestern Arabia, Sudan, Sinai, and the Eastern Desert of Egypt (Hamimi et al., 2020a). The granitic rocks of Egypt have been generally divided into two main classes comprising older grey granites (750–610 Ma) and younger granites (610–580 Ma) (Akaad and Noweir, 1978, El-Gaby et al., 1984, El Ramly, 1972, Hamimi et al., 2020a, Hussein et al., 1982). Younger granites are widely distributed within the Egyptian shield and represent essential sources of Sn–W, Au, and Nb–Y–REE mineralizations (Ahmed, 2022, Hassan and Hashad, 1990, Stern, 1979).

Egyptian granites, for example, albitized granites, have long been precious sources of various mineral resources such as Li, F, Zr, Nb, Sn, Ta, W, Pb, U, Th, and rare earth elements (REE) (Linnen et al., 2012, Moussa et al., 2021, Neto et al., 2009). The Eastern Desert of Egypt recorded more than 16 occurrences of albitized granite hosting rare metals mineralization (Aboelkhair et al., 2010, Sabet et al., 1976c, Zoheir et al., 2020). These albitized granites commonly exhibit some general characteristics: small size (1–3 km^2 in their outcrop), commonly associated with larger granitic plutons; lens-like (Humr Waggat, Ineigi, Umm Naggat), domal (Nuweibi, Muelha, Zabara, Qash Amir) or stock-shaped occurrence (Igla, Abu-Dabab) (Abd-Elmeguid et al., 2003, Aboelkhair et al., 2010, Azer et al., 2019, El-Qassas et al., 2021, El–Afandy et al., 2000, Gaafar, 2015, Gaafar and Ali, 2015, Hassanen et al., 2008, Moussa et al., 2021, Sabet, Tsogoev, 1976c, Zoheir et al., 2020). Rare metals deposits are mostly related to magmatic activity; however, the majority of them have been enriched through later-stage metasomatic hydrothermal albitization processes, and are typically associated with extensively-dissected structural zones (Abuamarah et al., 2021, Azer et al., 2019, Moussa et al., 2021, Zoheir et al., 2020).

As an efficient tool for lithological and structural mapping, remote sensing has been effectively used for hydrothermal alteration delineation at various spatial scales (Abrams and Yamaguchi, 2019, Ali-Bik et al., 2022a, Ali-Bik and Hassan, 2022, Bishta and Sonbul, 2021, Dawoud et al., 2017, Frutuoso et al., 2021, Gabr et al., 2021, Gad and Kusky, 2007, Hassan et al., 2022, Ninomiya et al., 2005, Pour et al., 2019). Remote sensing has been increasingly utilized for detecting these potentially mineralized rocks (Ali-Bik et al., 2022b, Cardoso-Fernandes et al., 2020a, Ewais et al., 2022, Govil et al., 2018, He et al., 2022, Imran et al., 2022, Mahdi et al., 2022, Peyghambari and Zhang, 2021, Pour et al., 2018, Qasim et al., 2022, Rajan Girija and Mayappan, 2019, Rokos et al., 2000, Shirazy et al., 2018, Wambo et al., 2020, Yu et al., 2012). In contrast to conventional field surveying, mineral exploration employing remote sensing is less expensive, time-saving, and more efficient, especially in inaccessible arid regions with high-elevation, rugged terrains (El Kati et al., 2018, Gad and Kusky, 2007, Rajan Girija and Mayappan, 2019). Geological mapping techniques have evolved, and currently, the combination of remote sensing data with innovative data science, such as machine learning, is attracting considerable interest due to its impressive results (Bachri et al., 2022, Cardoso-Fernandes et al., 2020b, Cracknell and Reading, 2014, El Fels and El Ghorfi, 2022, Han et al., 2022a, Köhler et al., 2021, Manap and San, 2022b, Shebl et al., 2021b, Shebl and Csámer, 2021a, Shebl and Csámer, 2021c, Shirmard et al., 2022a, Xiang et al., 2020).

One of the outcomes of remote sensing images, most frequently anticipated, is accurate thematic classification. Recent efforts to increase the dependability and precision of imagery classification have resulted in the development of machine learning classification systems. In order to manage multi-layer data with complex characteristics, machine learning, a subcategory of artificial intelligence, is finding increasing use in geostatistical remote sensing (Rodriguez-Galiano et al., 2015, Varouchakis et al., 2021). Through time, several geologists have made remote sensing data more effective in lithological and mineral mapping by employing advanced data analysis techniques such as machine learning algorithms (Bachri et al., 2019, Costa et al., 2019, Han et al., 2022b, Harvey and Fotopoulos, 2016, Santos et al., 2022, Shebl et al., 2021b, Shebl and Csámer, 2021c, Shirmard, Farahbakhsh, 2022a, Shirmard et al., 2022b, Wu et al., 2021, Xi et al., 2022). Integrating remote sensing data of different spectral, spatial, and temporal

Table 1
Characteristics of ASTER and Sentinel-2 Data.

ASTER				Sentinel-2			
Band	Spectral region	Central wavelength (μm)	Spatial resolution (m)	**Band**	Spectral region	Central wavelength (μm)	Spatial resolution (m)
1	VNIR	0.560	15	**1**	Ultra blue	0.443	60
2		0.660	15	**2**	Blue	0.490	10
3N		0.820	15	**3**	Green	0.560	10
3B		0.820	15	**4**	Red	0.665	10
4	SWIR	1.650	30	**5**	VNIR	0.704	20
5		2.165	30	**6**	VNIR	0.740	20
6		2.205	30	**7**	VNIR	0.782	20
7		2.260	30	**8**	VNIR	0.842	10
8		2.330	30	**8a**	VNIR narrow	0.865	20
9		2.395	30	**9**	SWIR water vapor	0.945	60
10	TIR	8.291	90	**10**	SWIR cirrus	1.375	60
11		8.634	90	**11**	SWIR	1.610	20
12		9.075	90	**12**	SWIR	2.190	20
13		10.657	90				
14		11.318	90				

VNIR = visible near infrared, SWIR = short wave infrared, and TIR = thermal infrared

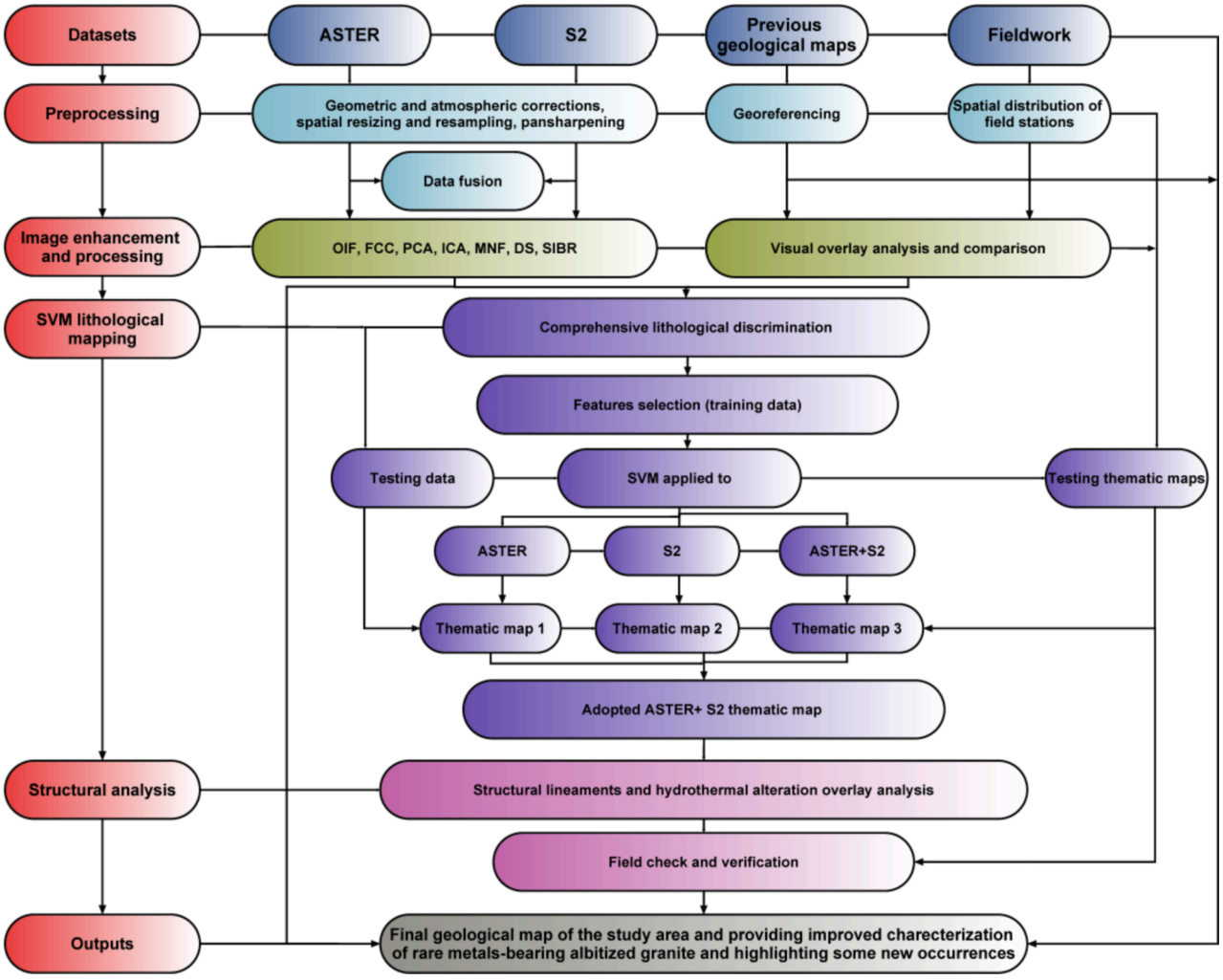

Fig. 2. Flowchart showing the used materials and followed methodology in the current study.

resolutions with machine learning algorithms and geological field surveying has helped overcome many exploration challenges such as subjective judgment, climate conditions, topography, and operating approaches that can result in unreliable mapping and misleading prospection (Latifovic et al., 2018, Sang et al., 2020, Shirmard, Farahbakhsh, 2022b).

Consequently, the current study combined various remote sensing data (ASTER and Sentinel-2) processed using different techniques and analyzed utilizing the Support Vector Machine algorithm (SVM) for detailed lithological and hydrothermal alteration mapping of the Umm Naggat area. The resultant thematic geological map has been verified through intensive fieldwork and highlighted non-reported potential

Table 2
Training and Testing Data Used for The Lithological Allocation.

Class Number	Class	Training Data		Testing Data	
		Pixels	Percentage (%)	Pixels	Percentage (%)
1	ABG	1056	79.69	269	20.30
2	BG	1077	76.32	334	23.67
3	OMV	1004	78.74	271	21.25
4	TRA	346	75.54	112	24.45
5	AMV	1112	75.13	368	24.86
6	OGR	938	75.46	305	24.53
7	SP	321	78.10	90	21.89
8	BMV	1586	77.21	468	22.78
9	MSD	1458	75.00	486	25.00
10	MGD	1458	75.00	486	25.00
11	WD	1068	75.21	352	24.78
12	HYD	1005	79.50	259	20.49
13	ALK	1003	78.48	275	21.51

Albitized Granite (ABG), Biotite alkali feldspar Granite (BG), Ophiolitic Metavolcanics (OMV), Trachyte (TRA), Acidic Metavolcanics (AMV), Older Granite (OGR), Serpentinite (SP), Basic Metavolcanics (BMV), Metasedimentary Rocks (MSD), Metagabbro-Diorites (MGD), Alkali Granite (ALK), Wadi Deposits (WD), and Hydrothermal Alteration (HYD).

mineralized zones of albitized granite. In addition, this study cross-links hydrothermal alteration zones, high-density structural zones, and albitized granite distribution to propose new exploration targets for rare metal (Ta-Nb-Sn) mineralization in the study area.

2. Study area and geological setting

Umm Naggat area consists mainly of Precambrian igneous and metamorphic basement rocks. It is located in the Central Eastern desert of Egypt between latitudes 25° 27″N and 25° 32″N and longitudes 34° 10″E and 34° 19″E (Fig. 1). Based on field investigation and previous studies (Abd El Nabi, 2012, Al-Arifi et al., 2021, El-Qassas et al., 2021, El–Afandy, Abdalla, 2000, Gaafar, 2015, Gaafar et al., 2022, Gaafar and Ali, 2015, Hassanen, Moghazi, 2008), Umm Naggat area consists of three principal litho-tectonic units, including (1) ophiolitic mélange (serpentinites, metagabbro-diorites, ophiolitic metavolcanics), (2) island-arcassemblage (arc metavolcanics, metasedimentary rocks, older granites), (3) late to post-collision assemblage (younger granites, trachyte plugs, dykes).

Serpentinites (SP) are massive fine-grained rocks that exhibit dark green, olive green, and occasionally black colors. SP mostly form lenticular bodies cropping out in the northern parts of the study area, where they have tectonic contact with metasedimentary rocks (MSD). Metagabbro-diorites (MGD) occur as dark green to blackish green massive rocks exposed locally in the eastern and southeastern corners of the study area. MGD form moderate relief terrains and have sharp intrusive contacts with the younger granite.

Metavolcanics (MV) were generally classified as older metavolcanics which were a component of an ophiolite association, and younger metavolcanics belonging to the island-arc association (El-Gaby et al., 1988, Stern, 1981). MV occur as dark brown rocks in several localities in the western and eastern parts of the Umm Naggat area, and they are distinguished based on the moderate to high relief. Arc metavolcanics are widely distributed as a nearly-continuous belt in the eastern part of the study area; they comprise acidic to basic varieties (Abd El Nabi, 2012). In contrast, ophiolitic metavolcanics (OMV) have limited occurrence on the western side. MV are frequently intruded by younger granite with sharp intrusive boundaries.

Metasedimentary rocks (MSD) in Umm Naggat area are exposed mainly as a narrow belt extending in NW-SE direction in the northeastern part of the study area. They are intercalated with metavolcanics and occasionally intruded by younger granite with sharp intrusive contacts. Older granites (OGR) are found as low-relief hills and are characterized by exfoliation structures. They occur as fine- to medium-grained varieties exhibiting a spectrum of pale grey colors. Older granites essentially cover the southeastern and southwestern corners of the study area; however, small scattered localities were recorded along the northern, eastern, and western sides. Older granites are frequently intruded by younger granites with sharp intrusive contacts.

Umm Naggat younger granite (UNYG) pluton represents the highest relief, oval-shaped core of Umm Naggat area. According to field investigations and previous studies (Abd El Nabi, 2012, Al-Arifi, El-Din, 2021, El-Qassas et al., 2021, El–Afandy, Abdalla, 2000, Gaafar, 2015, Gaafar, Elbarbary, 2022, Gaafar and Ali, 2015), UNYG comprises three distinct granitic units; biotite alkali feldspar granite, alkali granite, and albitized granite. UNYG has irregular boundaries and frequently sends offshoots into the surrounding metavolcanics, metagabbro-diorites, and older granites. Biotite alkali feldspar granite (BG) mainly outcrops in the southern part of the UNYG pluton as a 14 km^2 body extending in an E-W direction; however, some scattered occurrences were recorded in the northwestern corner of the investigated area. BG is a coarse-grained rock that exhibits a buff color and occasionally hosts several enclaves of older metagabbro-diorites along their contacts. The alkali granite (ALK) outcrops in the middle part of the pluton towards the north relative to BG. The ALK intrudes BG with nearly vertical sharp contacts and moderate reliefs (Al-Arifi, El-Din, 2021).

In comparison to previous studies (Abd El Nabi, 2012, Al-Arifi, El-Din, 2021, El-Qassas et al., 2021, El–Afandy, Abdalla, 2000, Gaafar, 2015, Gaafar and Ali, 2015) which reported that albitized granite (ABG) is exposed as dome-shaped protrusions or cupolas only in the northern part of UNYG, our field investigations revealed that albitized granite (ABG) is widely distributed in the southern, northern parts and towards the west of UNYG. ABG in the northern and southern parts commonly

Table 4
Optimum Index Factor Index Highest Rankings of ASTER VNIR-SWIR Bands.

R	G	B	Ranking
b1	b5	b9	85.17
b1	b6	b9	84.72
b1	b4	b9	84.38
b1	b5	b8	84.16
b1	b5	b7	84.09

Red (R), Green (G), and Blue (B).

Table 3
Optimum Index Factor Correlation Matrix of ASTER VNIR-SWIR Bands.

Band (b)	b1	b2	b3	b4	b5	b6	b7	b8	b9
b1	1	0.99	0.98	0.92	0.9	0.9	0.91	0.9	0.88
b2	0.99	1	0.99	0.94	0.91	0.91	0.93	0.93	0.91
b3	0.98	0.99	1	0.95	0.92	0.92	0.94	0.95	0.92
b4	0.92	0.94	0.95	1	0.98	0.97	0.96	0.96	0.95
b5	0.9	0.91	0.92	0.98	1	0.99	0.96	0.95	0.96
b6	0.9	0.91	0.92	0.97	0.99	1	0.96	0.96	0.96
b7	0.91	0.93	0.94	0.96	0.96	0.96	1	0.99	0.97
b8	0.9	0.93	0.95	0.96	0.95	0.96	0.99	1	0.98
b9	0.88	0.91	0.92	0.95	0.96	0.96	0.97	0.98	1

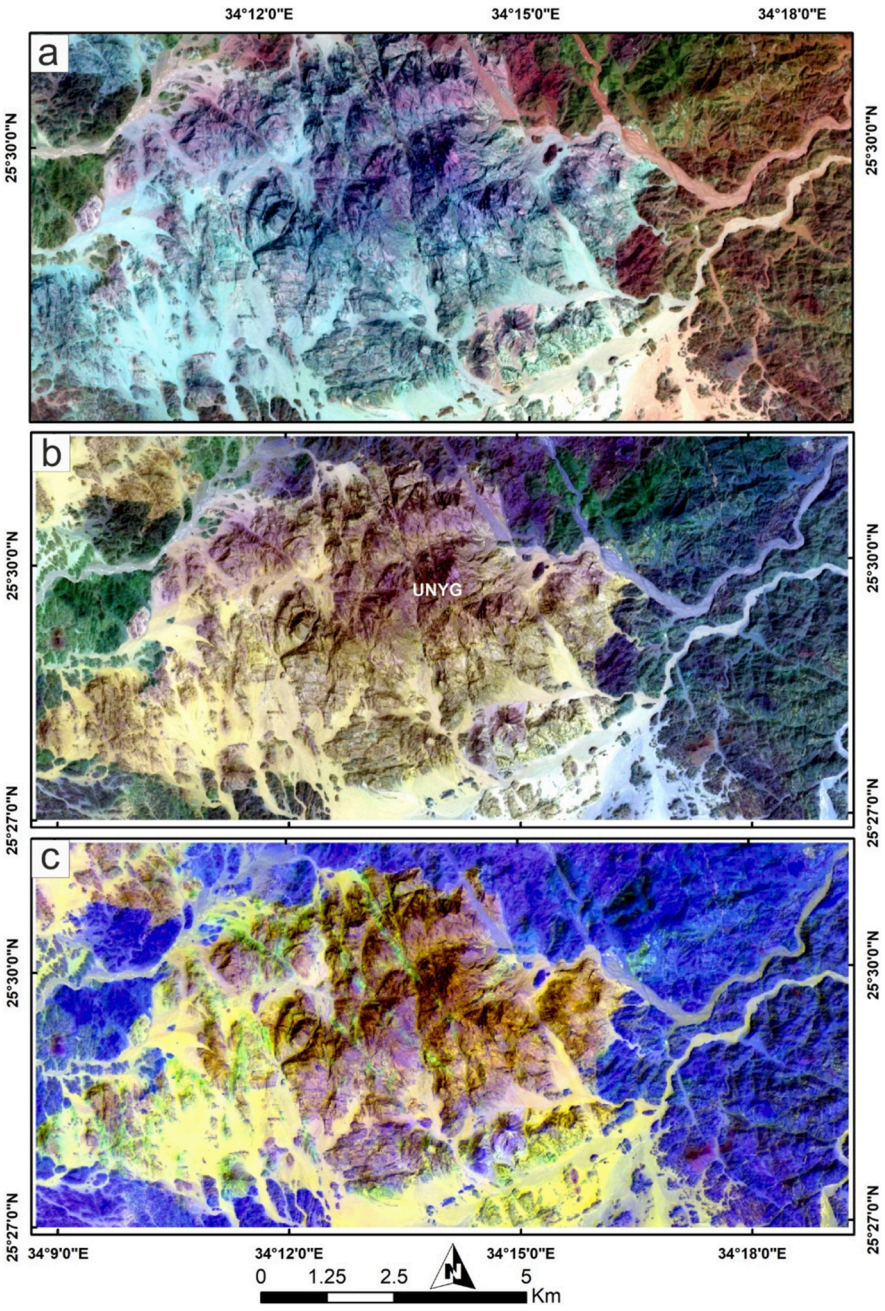

Fig. 3. lithological discrimination using ASTER (a) VNIR-SWIR OIF of b1-b5-b9 in RGB, and false color composites of (b) VNIR-SWIR b8-b5-b1 in RGB, and (c) SWIR-TIR b8-b4-b12.

extends in an E-W direction, possessing irregular boundaries and moderate to high reliefs. ABG in the northern portion of the UNYG pluton has undergone massive post-magmatic metasomatism, resulting in the formation of Zr, Nb, Ta, U, Th, F, and albite-enriched granite greisen body (Abd El Nabi, 2012, Naim et al., 1996). In addition, disseminated tantalite and columbite are the primary ore minerals; however, cassiterite is present in minor amounts, as well as thorite and zircon (Naim, EI Miligy, 1996). Locally, ABG is followed by fluoritization and kaolinization. At the northern, eastern, and western exocontacts of the UNYG, small apophyses of albitized granites dissected the country rocks. Pegmatites frequently occur as lens-shaped bodies at the margins of albitized granite. Gaafar and Ali (2015) reported pegmatites to be rich in Nb-Ta mineralizations with garnet and fluorite.

Several Cretaceous-Paleogene trachyte (TRA) dykes and plugs cut through UNYG in NW-SE and E-W directions (Abd El Nabi, 2012, Meneisy, 1990). Structurally, the UNYG is affected by numerous fault systems, quartz veins, and dyke swarms in different directions, such as NNW, NE, N-S, E-W, and NW (El Shazly, 1964, Naim et al., 1996). Hydrothermal alterations occur mainly in NW, NNW, NNE, and N-S directions. For instance, Kaolinization, greisen alteration, and green to violet fluorite veins were recorded (Gaafar, 2015).

3. Materials and methods

3.1. Remote sensing data

In the present work, Advanced Spaceborne Thermal Emission and Reflection Radiometer (ASTER) and Sentinel-2A (S2) satellite imagery provided remote sensing data. In this study, both ASTER and Sentinel-2A images, acquired in March 2004 and August 2021, respectively,

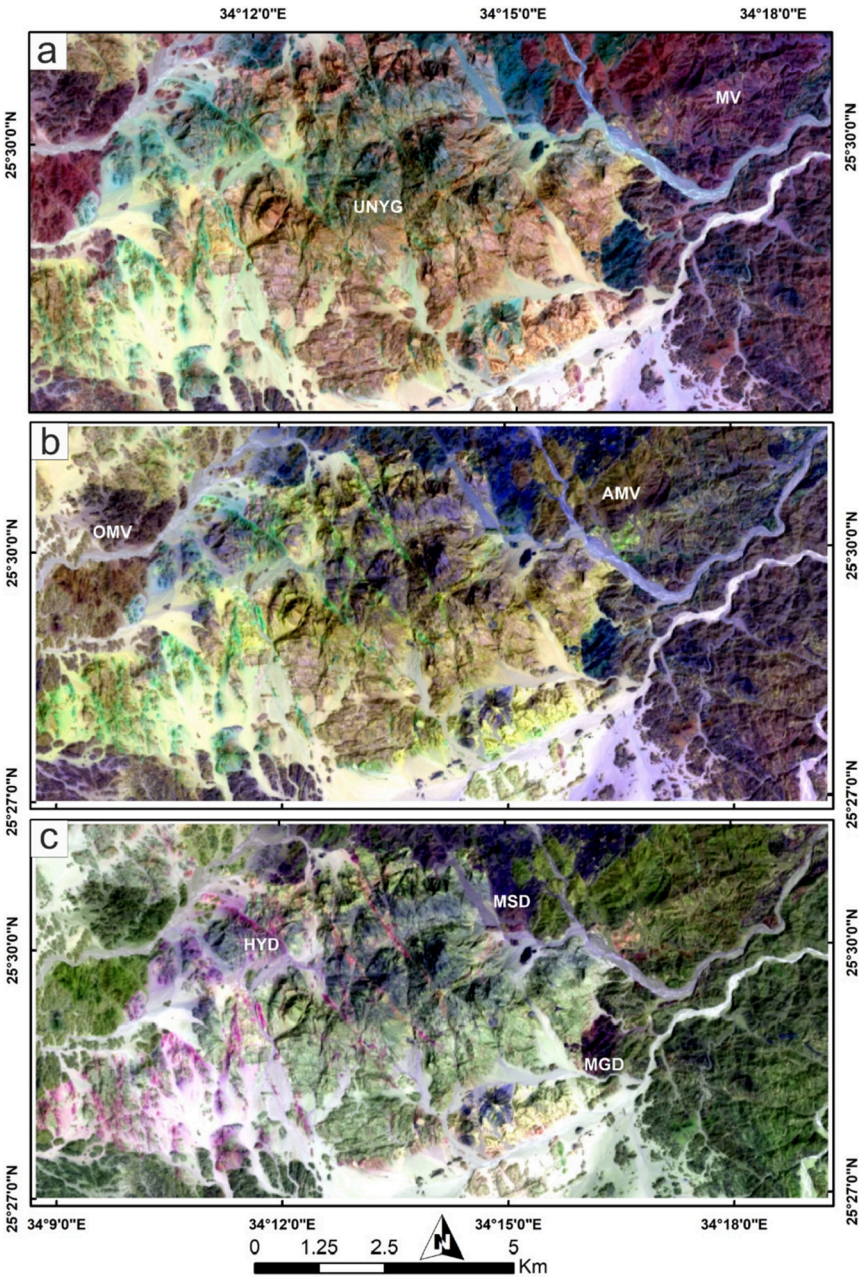

Fig. 4. Lithological discrimination using Sentinel-2 FCCs of (a) b12-b6-b2, (b) b12-b11-b2, and (c) b11-b12-b7 in RGB.

were utilized.

ASTER is an imaging tool aboard the Terra satellite, which was released as part of NASA's Earth Observing System package in December 1999. The combination of 14 narrow-width bands, reasonable spatial and spectral resolutions in the visible near-infrared (VNIR), short-wave infrared (SWIR), and thermal infrared (TIR) regions makes ASTER data the best choice for geological mapping with various purposes (Abdeen et al., 2001, Abrams and Yamaguchi, 2019, Bedell, 2001, Rowan and Mars, 2003, Volesky et al., 2003) (Table 1). Particularly, the ASTER shortwave infrared (SWIR) channels markedly improve the spectral characterization of minerals and rock units of the Earth's surface (Crosta et al., 2003, Gabr et al., 2015, Gad and Kusky, 2006, Hassan and Sadek, 2017, Hassan et al., 2015, Ninomiya, Fu, 2005, Ninomiya et al., 2006). However, the short-wave infrared channels of ASTER stopped their operation in April 2008 due to the failure of the cryocooler (Liang, 2018).

Supplementing ASTER data, Sentinel-2 (S2) data were utilized for better lithological discrimination due to its higher spatial resolution indicated by several results over similar terrains (Fal et al., 2019, Moghtaderi et al., 2022, Salehi et al., 2019, Shebl et al., 2021b, Tompolidi et al., 2020). Despite having fewer SWIR bands than ASTER, S2 was utilized effectively for improving the spatial resolution of ASTER color composites and delivering more accurate classification results using machine learning methods. Sentinel-2 satellites are equipped with Multi-Spectral Instrument (MSI) for imaging the ground at nearly 786-km elevation (Drusch et al., 2012). The S2 image contains thirteen spectral bands in the VNIR and SWIR spectral ranges (Drusch et al., 2012) (Table 1).

The two datasets were preprocessed and resized to the boundaries of the study area. Cloud-free level-1 T ASTER data in this study were resampled to 10 m spatial resolution, layer stacked, and atmospherically corrected using the FLAASH (Fast Line of Sight Atmospherics Analysis of Hypercubes) module to remove water vapor and cloud effects and to obtain surface reflectance from the digital counts. The Sentinel-2

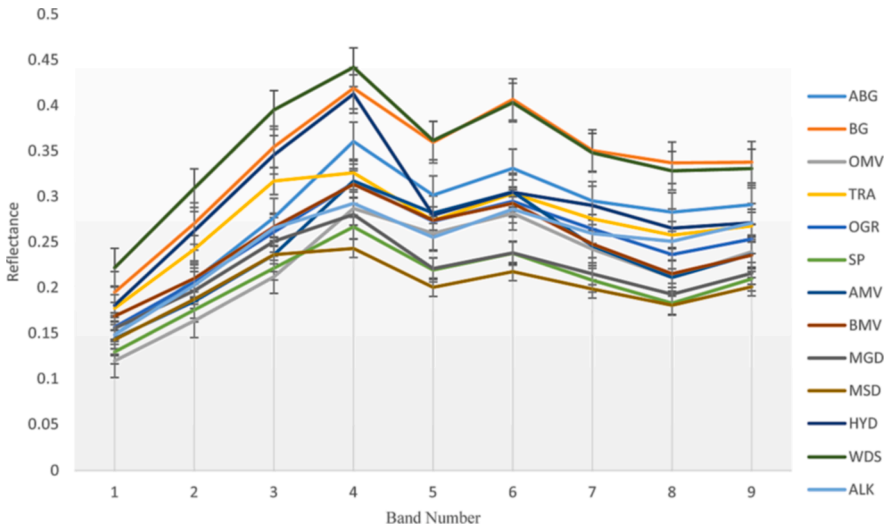

Fig. 5. Average spectral reflectance of the classified lithological classes in the study area including albitized granite (ABG), biotite alkali feldspar granite (BG), ophiolitic metavolcanics (OMV), trachyte (TRA), acidic metavolcanics (AMV), older granite (OGR), serpentinite (SP), basic to intermediate metavolcanics (BMV), metasedimentary rocks (MSD), metagabbro-diorites (MGD), alkali granite (ALK), wadi deposits (wd), and hydrothermal alteration (HYD).

cloudless image was atmospherically corrected and orthorectified automatically using the ESA-provided Sentinel Application Platform (SNAP) software. After atmospheric correction, each image band was resampled cubically to 10 m spatial resolution and layered into a single file. All S2 bands with a pixel size of 60 m were not considered for further analyses due to their poor spatial resolution.

Regarding the methodology applied by Chen et al. (2022), ASTER and S2 data were fused using Gram–Schmidt pansharpening to improve ASTER's spectral and spatial resolutions. Chen, Zhao (2022) demonstrated that fusing the data of ASTER and S2 helps increase spatial resolution while preserving spectral consistency. Thus, it is a valuable and cost-effective technique for enhancing the identification precision of hydrothermal alteration minerals and differentiating rock units. The implemented materials and followed methodologies in this study area are demonstrated in the flowchart in Fig. 2.

3.2. Image processing techniques

Increasing the number of integrated image processing techniques over different datasets (ASTER and S2) could greatly help lithological discrimination and highlight lithological contacts. In the current study, several techniques employing diversified mechanisms for image enhancement are applied. These techniques include optimum index factor (OIF), false color composites (FCC), band rationing (BR), relative band depth (RBD), independent component analysis (ICA), principal component analysis (PCA), decorrelation stretch (DS), minimum noise fraction transform (MNF), and spectral indices ratios (SIR).

3.2.1. Optimum index factor (OIF)

The optimum index factor (OIF) analysis ranks all possible Red-Green-Blue (RGB) color combinations of multispectral remote sensing data based on its total variance and correlation coefficient (Chavez, 1984, Chavez et al., 1982, Shebl and Csámer, 2021a). OIF is calculated based on equation (1) (Chavez, 1984):

$$OIF = \frac{\sum_{K=1}^{3} S_K}{\sum_{J=1}^{3} Abs(R_J)} \quad (1)$$

where R**J** is the absolute value of the correlation coefficient between any two of the three bands which are being evaluated, and S**k** denotes the standard deviation for band K. In our research, OIF ranks all the possible three RGB band combinations that can be produced using the first nine bands of ASTER data. The highest OIF value combination is typically considered to have the most information and is thus utilized for better lithological distinction.

3.2.2. False color composite (FCC)

A color composite image is generated by selecting spectral properties that improve the discrimination of lithological and hydrothermal alteration zones (Campbell and Wynne, 2011). FCC dramatically facilitates the visualization of the images to achieve better interpretation. In the current research, the selected RGB combinations are picked out regarding the type of exposed rock units, previous studies, OIF results, and spectral characteristics of the utilized datasets to ensure the highest level of differentiation.

3.2.3. Band ratios (BR)

The band rationing procedure is implemented by dividing one band's digital number (DN) values by the corresponding DN values of another band and projecting the resulting DN values as a grayscale image that provides relative band intensities (Sabine, 1999, Sabins and Floyd, 1986). In harmony with previous studies (Aboelkhair et al., 2010, Amer et al., 2012, Asran et al., 2017, Pour and Hashim, 2011), the current investigation demonstrated how BR transformations are beneficial for accurate lithological discrimination and qualitative detection of hydrothermal alteration within the study area.

3.2.4. Relative absorption band depth (RBD)

Relative Band depth (RBD) is the ratio between the total of the bands at the shoulders of a defined absorption peak and the band nearest to the peak (Mars and Rowan, 2006). RBD is an efficient three-point ratio formulation for determining diagnostic mineral absorption characteristics (Shebl et al., 2021a). In the current study, ASTER RBD images represent the sum of multiple data channels from both absorption bands divided by the minimum absorption band to reveal lithological dissimilarities (Crowley et al., 1989).

3.2.5. Principal component analysis (PCA)

Principle Component Analysis (PCA) is a known dimensionality reduction method where the first principal component accounts for the maximum possible data variability. Thus, the first principal components have the greatest variance possible (Pearson, 1901, Sabins, 2007), and are primarily used to build robust color composites, improving the visual interpretation of surface material mapping (Yamaguchi and Naito, 2003). The current research utilized the first principal components for

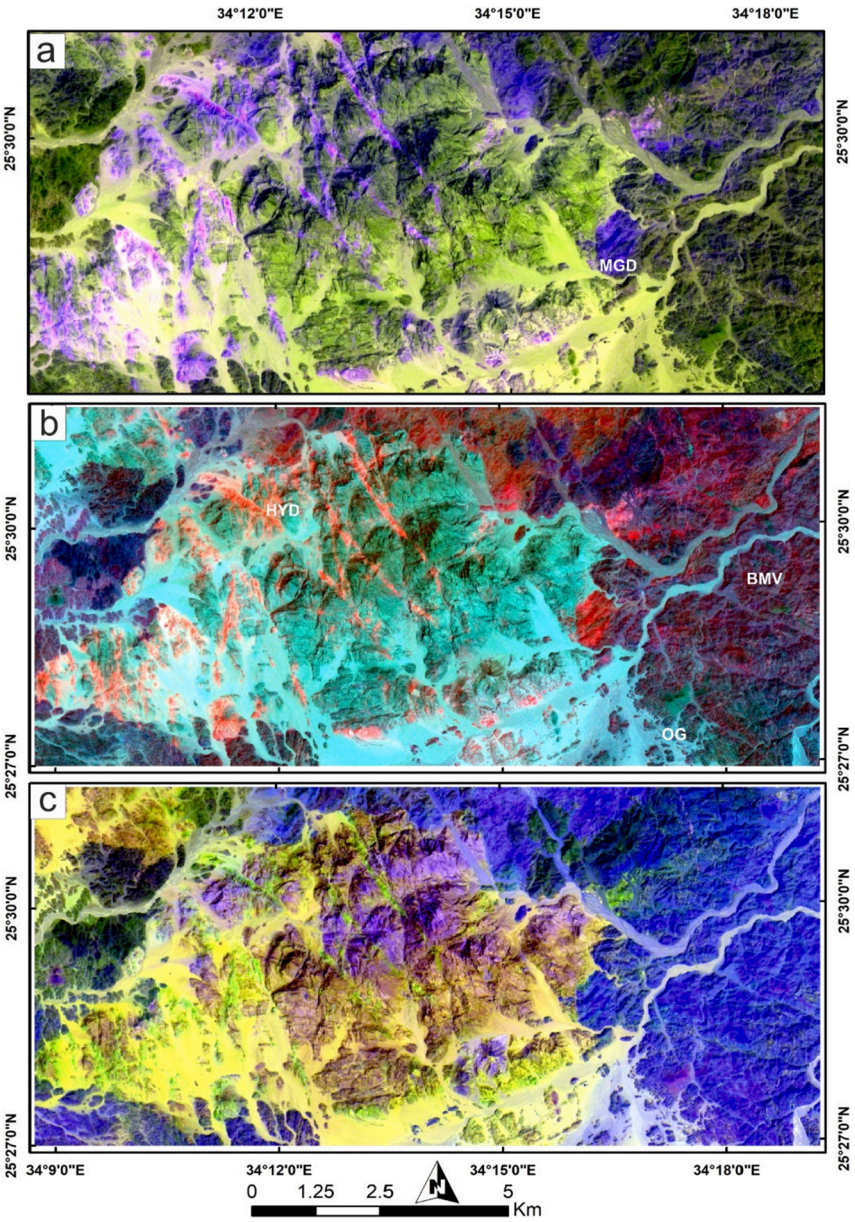

Fig. 6. Lithological characterization utilizing ASTER band ratios color composites of (a) b4-b6-b4/b5, (b) b4/b6-b8-b5, and (c) b8-b4-b1/b4 in RGB.

lithological discrimination, hydrothermal alteration mapping, and detecting major structural elements due to the higher amount of embedded information.

3.2.6. *Independent component analysis (ICA)*

ICA is a specific example of blind source separation (BSS) that distinguishes source signals from mixture signals with little or no prior knowledge of the source signals or mixing procedure (Cardoso, 1998). Consequently, the objective of ICA is to identify a group of uncorrelated elements that are as independent of one another as possible (uncorrelatedness is weaker than independence) (Yang and Cheng, 2015). Regarding several previous studies (Bentahar and Raji, 2021, Chen and Zhang, 1999, Kumar et al., 2020, Pour et al., 2019, Shebl et al., 2021b), the current study implements ICA for better lithological discrimination.

3.2.7. *Minimum noise fraction transform (MNF)*

The minimum noise fraction (MNF) approach refers to an orthogonal rotation that tends to result in components organized in increasing rank of random noise as opposed to decreasing rank of variance in principal components (Assiri, 2016, Green et al., 1988, Khan et al., 2007, Kruse et al., 2003). MNF usually involves two phases of PCA rotations; in the first phase, the principal components of the noise covariance matrix are determined, and the noise in the data is decorrelated and rescaled. The second phase involves extracting principal components from the noise-whitened data. The current research utilized the first MNF bands (possessing the most significant information) for lithological discrimination rather than following bands where noise increases progressively.

3.2.8. *Decorrelation stretch (DS)*

Decorrelation stretching involves processing the acquired data's primary components and yields a color composite image. This method optimizes the principal components of an image to generate a contrast stretch on the image to decrease the correlation between spectral bands. Since DS was successfully employed in lithological mapping (Abrams and Hook, 1995; Khan et al., 2007), it was used to distinguish between lithological units in the study area.

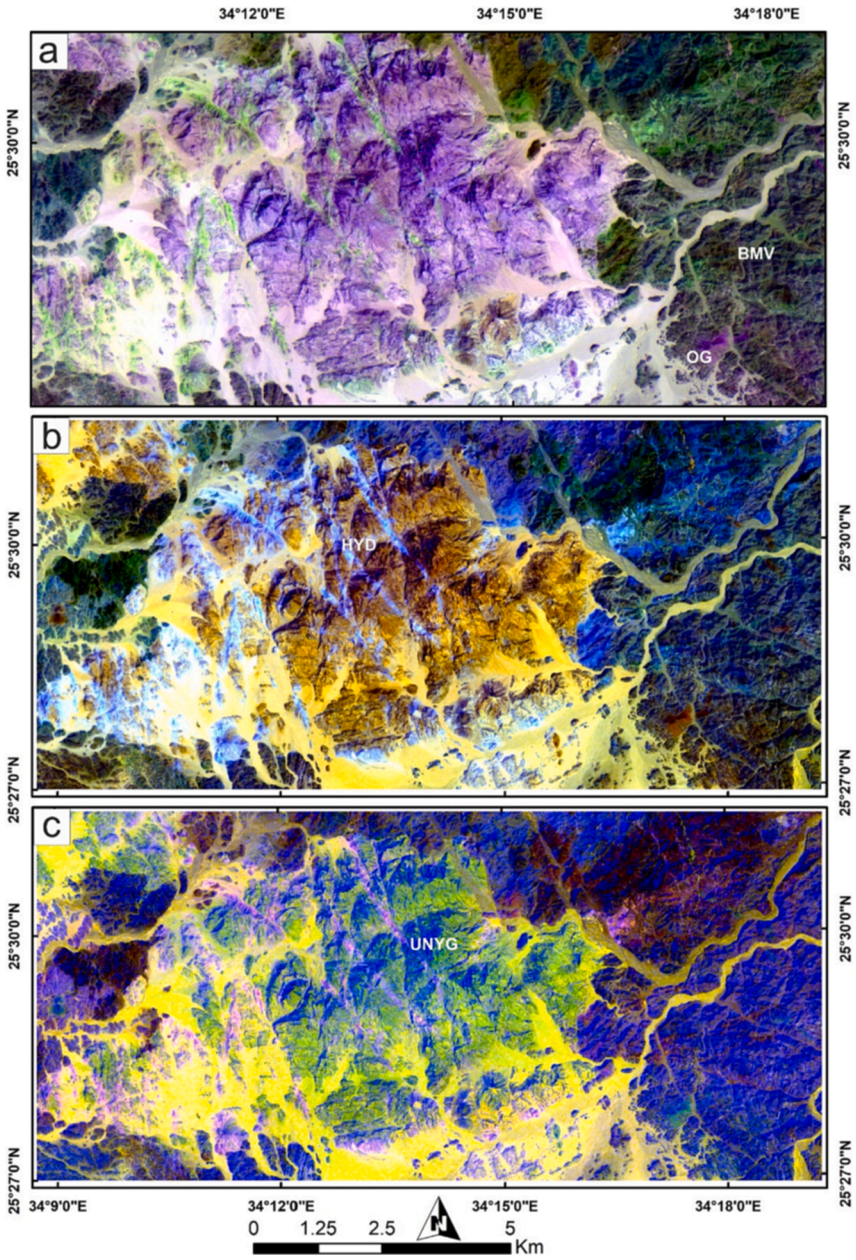

Fig. 7. Lithological characterization using ASTER band ratios color composites of (a) b8-b4-b9/b10, and (b) b8-b4-b4/b6 in RGB. (c) ASTER RBD color composite of b4-b8-RBD6 in RGB.

3.2.9. Spectral indices ratios (SIR)

Spectral indices are a type of orthogonal transformation used for mineral differentiation in exposed rocks using ASTER spectral bands (Yamaguchi and Naito, 2003). Yamaguchi and Naito (2003) developed the alunite, calcite, kaolinite, and brightness indices for SWIR data; Ninomiya (2004) defined the calcite index, the OH-containing altered mineral index, and the alunite index. Multiple spectral indices have been used for mineral exploration and ASTER-based mapping of alteration zones and have been proved to be effective (Bertoldi et al., 2011, Ding et al., 2014, Hassan and Ramadan, 2015, Hewson et al., 2001; Ninomiya et al., 2005; Rowan and Mars, 2003, Yajima and Yamaguchi, 2013).

In addition to image processing techniques, structural mapping was performed by automatically extracting lineaments from ASTER data using PCI Geomatica software. After applying PCA with the high-pass edge filtering technique to ASTER data, the first principal component attained nearly 97 % of the overall information extracted from the multispectral images. Thus, PCA1 was utilized in this analysis. Subsequently and using ArcGIS software, the density map was generated using the automatically derived lineaments. Several studies extracted the structural lineaments and their density over similar terrains automatically and various techniques verified the extracted features and that, in most cases, they are linked to mineral deposits (Abou El-Magd et al., 2015, Cooper, 2003, Hamimi et al., 2020b, Mohammadpour et al., 2020, Shebl and Csámer, 2021a, Shebl and Csámer, 2021b).

4. Machine learning classification

Digital image classification greatly enhances the objectivity of the image allocation procedure. However, other constraints prevented it from classifying data with the required degree of accuracy. Therefore, improving classification precision necessitates using multiple datasets and their combinations to get essential information on different rock types, leading to adequate generalization. Consequently, the current study seeks accurate and comprehensive lithological classification

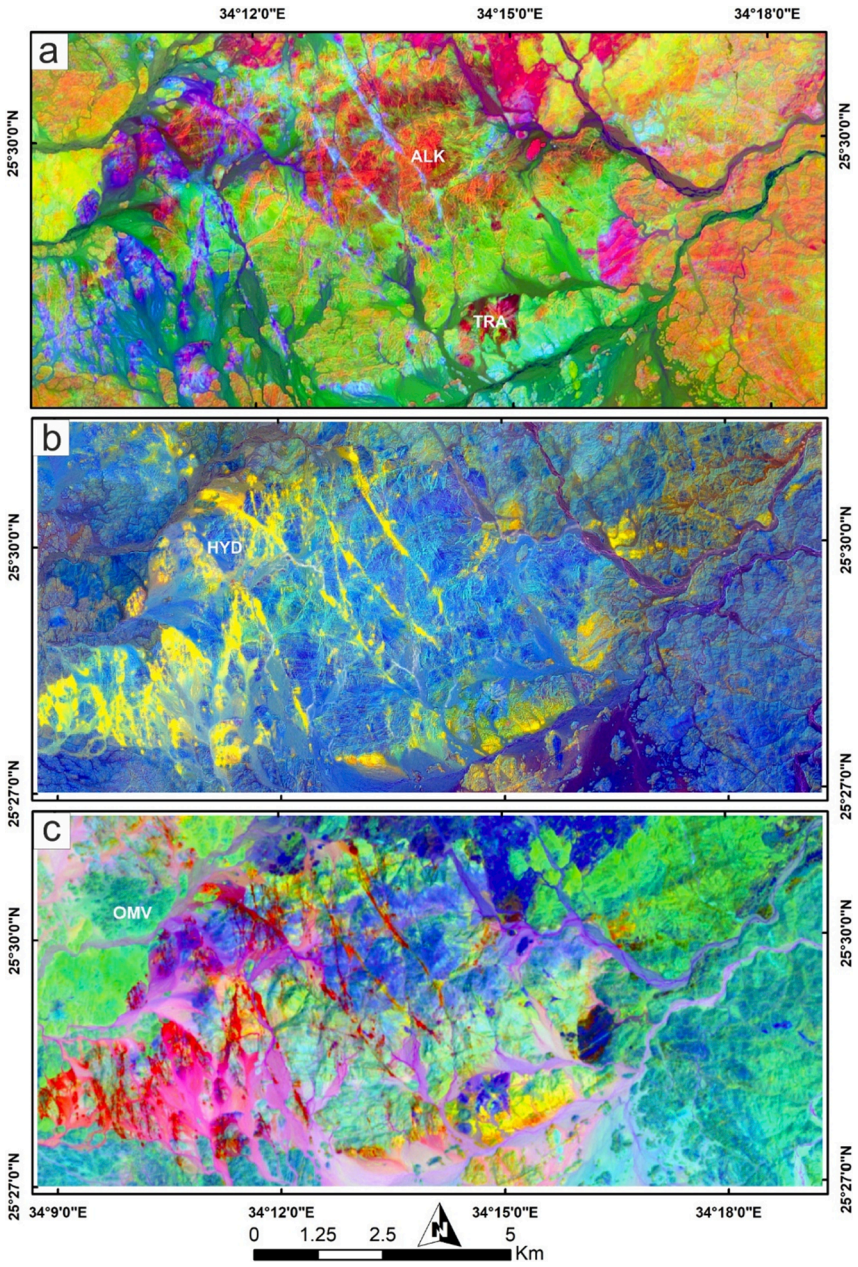

Fig. 8. Lithological characterization utilizing Sentinel-2 transformation techniques color composites of (a) PCA1-PCA2-ICA2, (b) ICA2-PCA3-PCA4, and (c) MNF1-MNF2-MNF3 in RGB.

through testing ASTER (AST), Sentinel-2 (S2), and ASTER + S2 (combined using the stacked-vector method (Shebl and Csámer, 2021c)) data and determining the most capable datasets for scrupulous lithological and hydrothermal alteration mapping of the widely-exposed basement rocks and their mineralized parts in Umm Naggat.

Ensuring adequate training and testing data, besides selecting a suitable classifier, are the main pillars for delivering veracious classification. Toward that aim, the outputs of all the previously mentioned image processing techniques, spectral signatures of different rock units, previous mapping, and field observations have been used as inputs for lithological classification utilizing the support vector machine algorithm. Support vector machine (SVM) has been used as the machine learning tool for the current study due to its potential and accuracy for mapping different rock types (Agrawal et al., 2022, Guha et al., 2022, Manap and San, 2022a, Youssef et al., 2022).

4.1. Training and testing data

The results obtained from remote sensing, field sampling, and previous geological maps were used as a reference for selecting the training and testing samples. The previous geological maps (1:100000–1:125000) were georeferenced and digitized in ESRI's ArcGIS software for more precise delineation of training and testing data after remote sensing mapping results. The georeferenced maps have an acceptable accuracy level, and reasonable total root mean square error (RMSE) (3.81). Furthermore, formerly processed remote sensing RGB images were imported to compare and correlate the lithologies through overlay analysis. For a more accurate selection of training sites, three shape files were digitized: (1) a lithology shape file comprising all lithological data from compiled previous geological maps, (2) several effective RGB color composites resulting from various image processing techniques, such as OIF, MNF, PCA, and BR (3) and a point shape file representing the locations of rock samples locations and their field

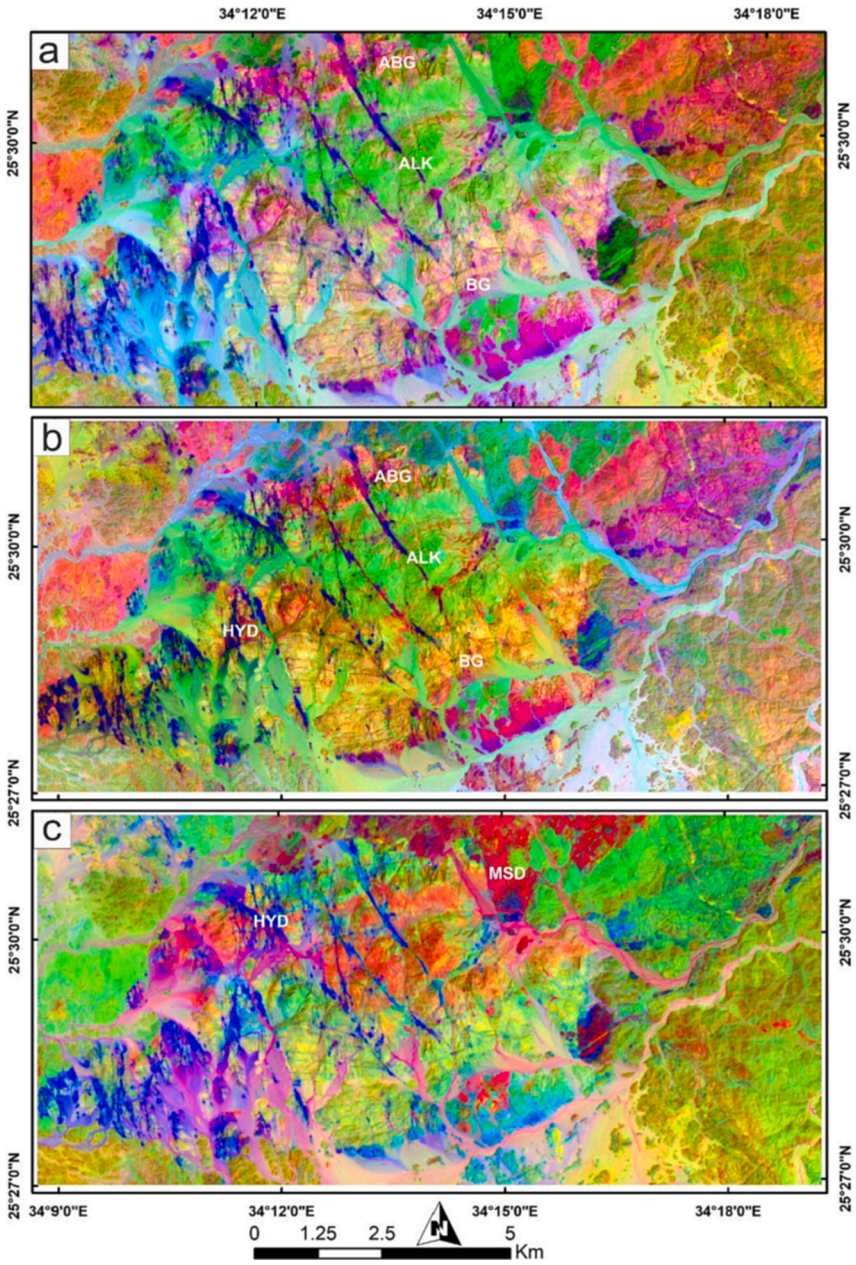

Fig. 9. Lithological characterization using Sentinel-2 minimum noise fraction and decorrelation stretch color composites of (a) MNF2-MNF3-MNF1, (b) MNF2-MNF3-MNF4, and (c) DS3-MNF2-b11 in RGB.

attributes. Consequently, careful, appropriate training areas, away from lithological boundaries, were defined for extraction of accurate lithological characteristics implementing 70–80 % and 30–20 % for SVM classification training and test sites for better consistency of results Kumar et al., 2020). Accordingly, training areas for thirteen lithological classes were determined and fed into the SVM algorithm. A total of 13,432 pixels representing thirteen lithological units were selected. Consequently, these pixels are divided into training and testing data (Table 2). The latter are randomly distributed, have never been seen by the classifier, and are used together with georeferenced field stations to verify the allocation process.

4.2. Support vector Machine (SVM)

The SVM is one of the most prominent supervised machine learning algorithms based on statistical learning (Cortes and Vapnik, 1995, De Boissieu et al., 2018, Mondal et al., 2012, Otukei and Blaschke, 2010). SVM classifier is highly regarded for its accuracy in classification since it is entirely focused on a rigorous mathematical model (Bachri et al., 2019; Perumal and Bhaskaran, 2010, Shebl et al., 2021b; Yu et al., 2012). In SVM, the fundamental strategy is to discover a hyper-plane that provides optimal separation between the two classes (Vapnik, 1995). This hyper-plane is produced using a subset of data stated as the training data set. The generalizability of the developed hyper-plane is confirmed using a subset of data known as the testing data set (Oommen et al., 2008, Vapnik, 1995). In lithological mapping, SVM was recommended by several previous studies (Maepa et al., 2021; Rodriguez-Galiano et al., 2015; Shabankareh and Hezarkhani, 2017, Shebl et al., 2022, Shebl et al., 2021b; Yu et al., 2012), since it has been confirmed to deliver higher classification accuracy than other traditional supervised classification schemes.

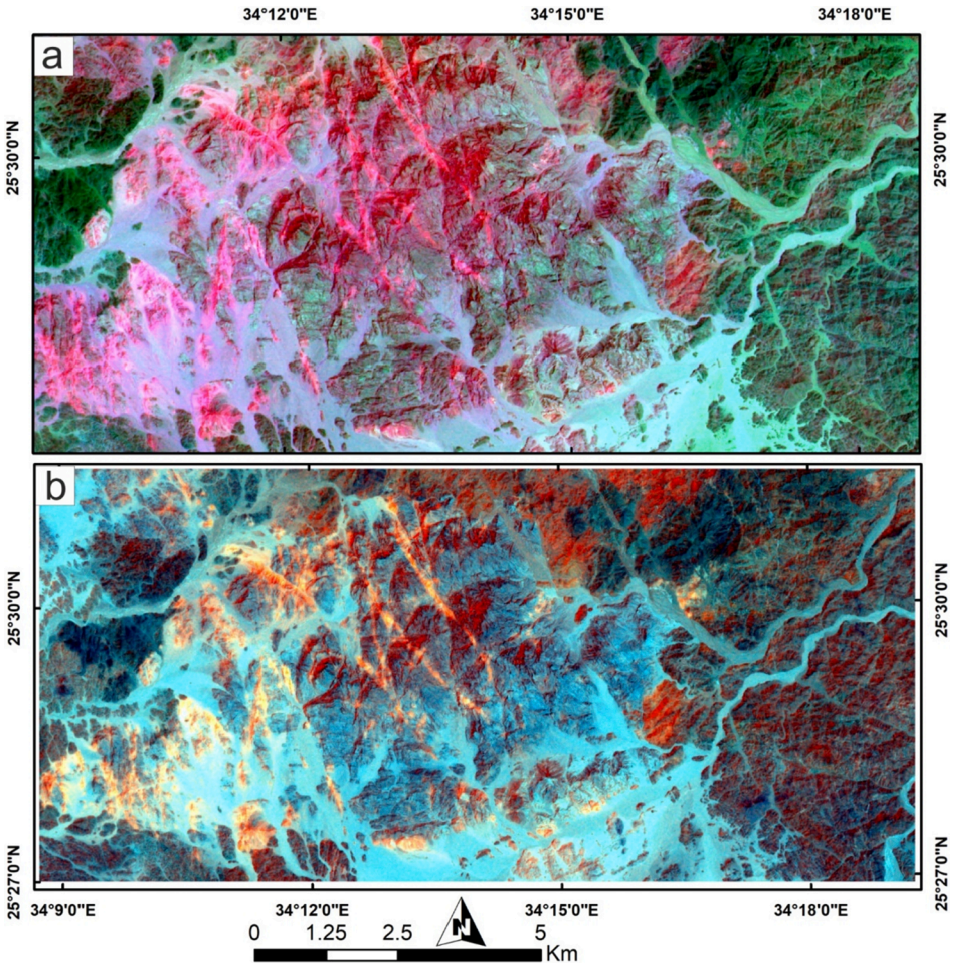

Fig. 10. Highlighting kaolinite and hydroxyl-bearing minerals using ASTER KLI and OHI color composites of (a) KLI-b1-b3, and (b) OHI-b4-b6 in RGB.

5. Results

5.1. Remote sensing results

5.1.1. Optimum index factor (OIF)

The OIF values demonstrate that ASTER bands have an extremely high ranking of 85.17 % (Tables 3, 4). OIF calculations indicate that the combination of bands b1-b5-b9 in RGB is the best selection for creating a color composite that contains the most information and exhibits the best lithologic separability in Umm Naggat area (Fig. 3a). This combination distinguished Umm Naggat's younger granite pluton (UNYG) from all the surrounding rock units in a sky bluish-violet color. Furthermore, using OIF results, other lithologic units could be recognized in greater detail. For instance, in the northeastern and northwestern parts of the study area, acidic arc metavolcanics were distinguished using a dark green tint; moreover the delineation of older granites, metasedimentary rocks, the metagabbro-diorite complex, serpentinites, and basic arc metavolcanics is also reasonable using the grades of reddish-brown color. Consequently, our results remarkably coincided with previous studies (Shebl and Csámer, 2021a) in highlighting OIF's effectiveness in separating the major rock units due to the utilization of bands with the least redundancy in remote sensing data.

5.1.2. False color composite (FCC)

Various FCC combinations show convenient lithological differentiation utilizing bands of ASTER (b8-b5-b1 and b8-b4-b12 in RGB respectively), or S2 (b12-b6-b2, b12-b11-b2, and b11-b12-b7 in RGB respectively). Agreeing with Shebl and Csámer (2021a) in utilizing SWIR and VNIR bands for better lithological discrimination in similar terrains, ASTER VNIR and SWIR combination (b8-b5-b1 in RGB) clearly distinguished the younger granite and metavolcanics of Umm Naggat from the nearby country rocks in yellowish beige and dark green tones, respectively. In addition, the former FCC categorized older granites, metasedimentary rock, serpentinites, and the metagabbro-diorite complex into a distinct violet color-coded group (Fig. 3b). Additionally, ASTER SWIR and TIR b8-b4-b12 in RGB represent the most useful FCC for defining UNGP. This combination displays the majority of lithologies in the same dark blue shade, except for the younger granite (in golden violet tint) (Fig. 3c).

Similarly, S2 FCC of b12-b6-b2 in RGB separated UNYG in buff color; metavolcanics and older granites in purple; metagabbro-diorites, serpentinites, and metasedimentary rocks in bluish-grey, while trachyte and hydrothermal alteration exhibited green tones (Fig. 4a). The S2 FCC image of b12-b11-b2 in RGB, which utilizes two SWIR bands, showed superior differentiation not only for rock units but also for hydrothermal alteration. Applying the former combination, the color of UNYG is yellowish-brown, whereas older granites were distinguished by their fuchsia rose hue in the southern parts of the study area. Additionally, two colors characterized metavolcanics towards the study area's eastern and western sides: acidic metavolcanics as greenish brown and basic to intermediate metavolcanics as greenish purple. Besides, dark blue metasedimentary rocks were distinguished from metagabbro-diorite, which appears in greenish blue, and serpentinites, which is displayed in brownish green. This FCC was also remarkably successful in detecting two types of hydrothermal alteration: green representing fault-related hydrothermal alteration and violet indicating hydrothermal alteration

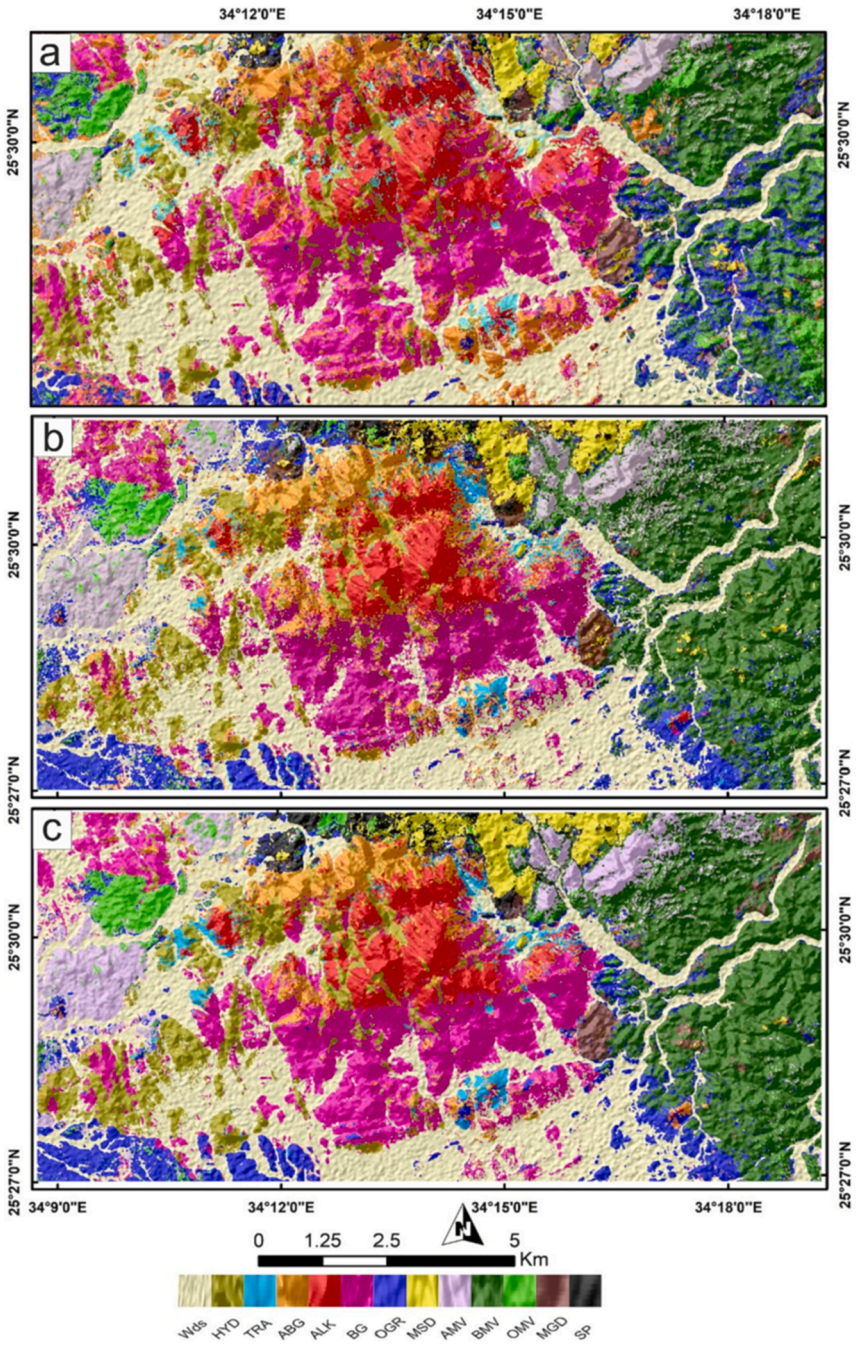

Fig. 11. Lithological thematic maps using SVM classification based on (a) Sentinel-2, (b) ASTER, and (c) ASTER + Sentinel-2.

(Fig. 4b). Additionally, assigning S2 b11-b12-b7 as FCC demonstrated a superior application for mapping trachyte plugs as an easily recognizable blue hue in the southern part of UNYG. It also improved the distinction of metagabbro-diorites in reddish-brown and metasedimentary rocks in violet-blue in the southeastern and northeastern parts of the study area. Furthermore, this FCC benefited the extraction of green serpentinites from northeastern metasedimentary rocks. As a fuchsia color, fault-related hydrothermal alteration is immediately noticeable (Fig. 4c).

Integrated ASTER and S2 results reveal important lithological information and help in detailed discrimination. Our results confirmed the role of SWIR bands of ASTER and S2 in lithological separation and identification of various forms of hydrothermal alteration (Fal et al., 2019; Kumar et al., 2015, Madani and Emam, 2011, Masoumi et al., 2017, Ninomiya, 2004, Shebl, Abdellatif, 2021a, Tangestani and Shayeganpour, 2020, Van der Meer et al., 2014).

5.1.3. *Band ratios (BR)*

Based on the spectral characteristics of the relevant surface material and its relative absorption to relative reflectance (Sabine, 1999), specified band ratios were selected. The extracted average spectral properties of Umm Naggat region lithological units are illustrated as absorption and reflection characteristics in Fig. 5, where most lithological units show strong absorption properties in ASTER b4, b5, b6, and b7 bands. Inspection of ASTER spectral characteristics and signatures of the exposed rocks demonstrates that band ratios of (b4/b5), (b4/b6), and (b1/b4) are advantageous in characterizing several lithological units. Displaying the band ratio b4/b5 in the blue channel of FCC b4-b6-b4/b5 in RGB highlights the mafic fingerprint of metagabbro-diorites, serpentinites as well as the iron-bearing alteration minerals in blue-violet

Table 5
Kappa coefficient, producer, user, and overall accuracies of the tested datasets.

Classes	S2		AST		S2 + AST	
	PA	UA	PA	UA	PA	UA
ABG	91.82	70.57	98.88	87.79	98.51	99.62
BG	84.73	95.29	71.86	99.59	81.14	96.79
OMV	76.75	77.61	96.68	96.68	98.52	96.39
TRA	42.86	63.16	91.96	91.96	94.64	100
AMV	73.88	97.54	95.52	95.52	97.76	100
OGR	91.48	77.72	89.51	84.52	95.41	93.27
SP	64.44	27.23	66.67	31.41	82.22	31.36
BMV	78.85	89.13	88.46	100	99.57	98.94
MSD	54.53	73.41	54.12	91.64	61.52	97.39
MGD	68.34	80.09	86.87	66.57	90.35	86.03
WD	99.43	89.29	100	75.21	100	83.41
HYD	97.68	95.83	99.23	100	100	98.48
ALK	90.18	75.15	100	100	99.64	100
Tot	**OA = 79.5**	**K = 0.77**	**OA = 86.6**	**K = 0.85**	**OA = 91.2**	**K = 0.90**

Support Vector Machine (SVM), Overall Accuracy (OA), kappa coefficient (K), Producer Accuracy (PA), User Accuracy (UA), Total number (Tot), Sentinel-2 (S2), and ASTER (AST).

hue (Fig. 6a). Using a band ratio b4/b6 in FCC b4/b6-b8-b5 in RGB, gives a comprehensive identification for the major rock units, where, it separates the boundaries of serpentinites in dark green in the north, younger granite in light green in the middle, and older granites in dark green with crinkled texture in the south (Fig. 6b). The band ratio b4/b6 further divides the eastern and western metavolcanics into three different varieties: acidic arc metavolcanics in blue, basic to intermediate arc metavolcanics in purple, and ophiolitic metavolcanics in blue-black in harmony with mapping results of previous studies (Abd El Nabi, 2012; Al-Arifi et al., 2021; El-Qassas et al., 2021, El–Afandy, Abdalla, 2000, Gaafar, 2015, Gaafar and Ali, 2015). In addition, FCC using both the b4/b5 and b4/b6 band ratios helped detect fault-related hydrothermal alteration in bright violet and orange colors (Fig. 6a, b).

The two ASTER SWIR bands of b8 and b4 proved to be extraordinarily useful when assigned with different band ratios in the three RGB channels, such as (b8-b4-b1/b4), (b8-b4-b9/b10), and (b8-b4-b4/b6). The band ratio of b1/b4 showed a unique advantage in characterizing lithium-bearing minerals such as spodumene and muscovite (Cardoso-Fernandes et al., 2019, Mashkoor et al., 2022). The color composite of b8-b4-b1/b4 in RGB impressively highlights hydrothermally altered potential Li-rich regions in bright violet color towards the north of the study area (Fig. 6c). The two band ratio color composites of b8-b4-b9/b10, and b8-b4-b4/b6 in RGB distinguished the distinct groups of Umm Naggat basement rocks (granitoids; metavolcanics; and metagabbro-diorites, metasedimentary rocks, serpentinites) (Fig. 7a, b).

Furthermore, metavolcanics are differentiated into two varieties utilizing the former combination of b8-b4-b9/b10 in RGB; acidic and basic to intermediate arc metavolcanics have dark green colors, while ophiolitic metavolcanics have a greenish-black tone (Fig. 7a). In complete harmony with previous studies (Bedell, 2001, Okada and Ishii, 1993, Rowan and Mars, 2003; Volesky et al., 2003), the current ASTER band-ratio combinations proved their effectiveness in lithological mapping due to their shown ability to highlight spectral properties of particular rocks and minerals while eliminating other types of information.

5.1.4. *Relative absorption band depth (RBD)*

Coinciding with (Crowley, Brickey (1989), Shebl, Abdellatif (2021a), our results confirmed the success of RBD in discriminating certain rocks and minerals. ASTER RBD6 combination of (b4 + b7)/b6 detected Al-OH absorption from muscovite or illite with high sensitivity (Crowley et al., 1989; Nair and Mathew, 2012, Rowan et al., 2005). Accordingly, isplaying RBD6 in the blue channel of FCC b4-b8-RBD6 in RGB helps identify granitic rocks as green due to their high-aluminum content. Furthermore, the former combination highlighted the hydrothermal alteration associated with hydroxyl and illite minerals in light-violet color (Fig. 7c).

5.1.5. *Principal and independent component analyses (PCA-ICA)*

As dimensionality reduction and image enhancement techniques, PCA and ICA transformations generate information-dense bands ideal for identifying the spectral features of minerals or rock units within the study area (Shebl et al., 2021b). Our results revealed that combining S2 PC1-PC2-IC2 in the RGB channels enhanced not only the differentiation of alkali granite in pale red color in the middle region of UNYG but also the identification of southern trachyte plugs in deep red color (Fig. 8a).

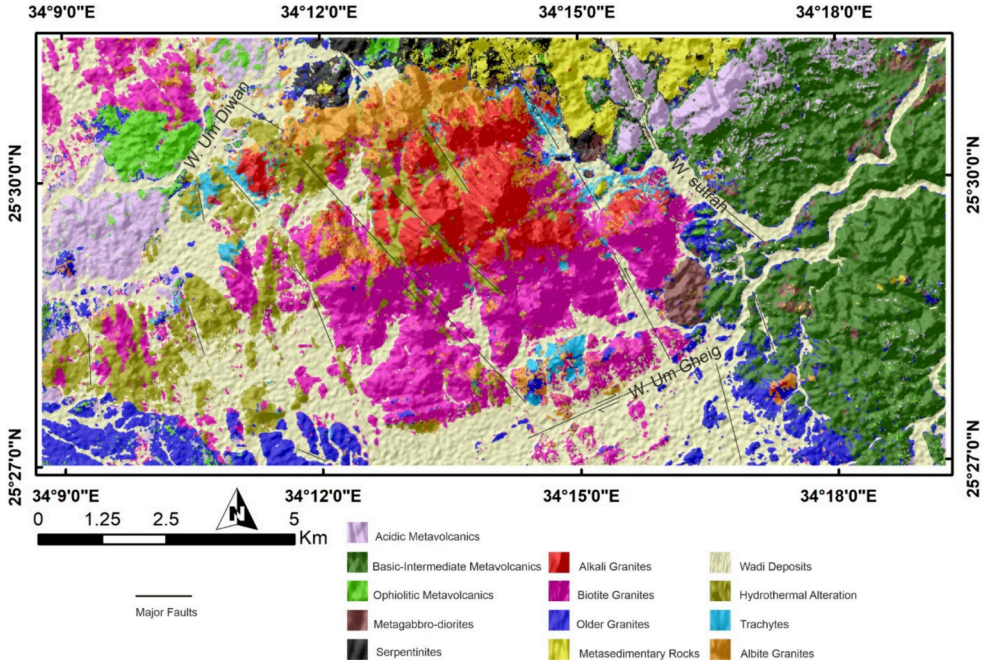

Fig. 12. Geological map of Umm Naggat area created using SVM based on ASTER and Sentinel-2 data.

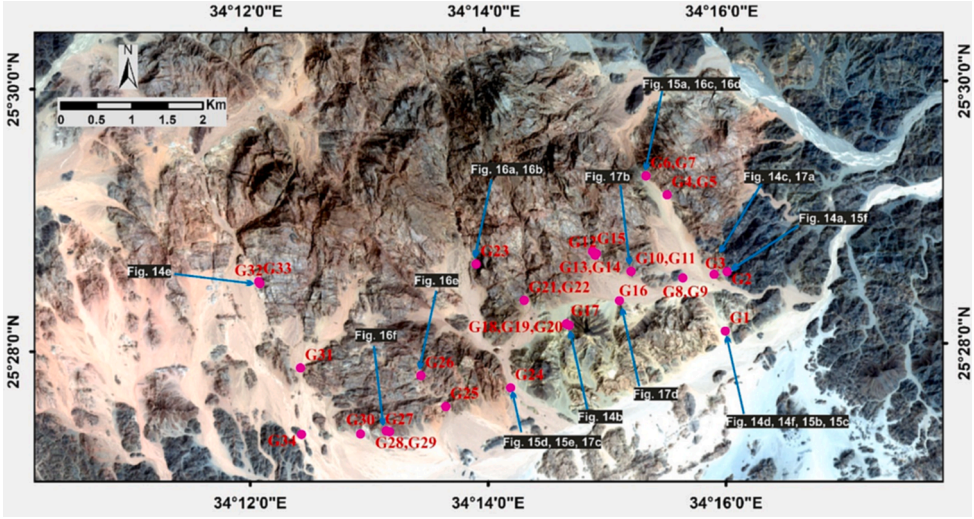

Fig. 13. Sentinel-2 image shows the field samples and figures locations in the study area.

Additionally, S2 RGB combination of IC2-PC3-PC4 demonstrated the tracts of hydrothermal alteration processes in yellow color affecting granitic rocks (Fig. 8b). The combined ICA - PCA technique demonstrates higher noise suppression capabilities when compared to using ICA or PCA separately (Berg et al., 2005). Consequently, these impressing results greatly recommend collective integration of S2 PCA and ICA for effective lithological and hydrothermal alteration mapping.

5.1.6. Minimum noise fraction (MNF) and decorrelation stretch (DS)

From a different perspective of image enhancement techniques, several attempts using MNF and DS over S2 data have been executed to significantly enhance the lithological discrimination within the study area. Our results revealed that the first few MNF bands, MNF1- MNF2- MNF3, MNF2- MNF3- MNF1, and MNF2- MNF3- MNF4 in RGB give excellent lithological differentiation as they carry the greatest amount of information, and less noise compared to subsequent bands. For instance, the MNF1- MNF2- MNF3 RGB image showed exquisite contrast between different rock units in the study area. This contrast enabled better detection of the ophiolitic metavolcanics as forest green color towards the west of UNYG (Fig. 8c). Moreover, using the first MNF bands as input for decorrelation stretch technique results in convenient discrimination for all the exposed rock units through DS of MNF3 (DS3)-MNF2-b11 FCC in RGB.

The final results of MNF and DS or their combined composite (MNFs 2–3-1, MNFs 2–3-4, DS3-MNF2-b11 in RGB) delivered a unique separation of the three types of younger granites and greatly resolved one of the significant issues of the current research related to albitized granite and hydrothermal alteration distribution within the study area. With MNF-DS results, fieldwork, and previous studies, the UNYG pluton was mapped into three different types: albitized granite (purple), alkali granite (green), and biotite alkali feldspar granite (yellow) (Fig. 9). Furthermore, these three combinations (MNFs 2–3-1, MNFs 2–3-4, and DS3-MNF2-b11 in RGB) were also exceptional in identifying and linking acidic arc metavolcanics between the eastern and western sides of the study area (Fig. 9).

5.1.7. Spectral indices ratios (SIR)

Regarding our target of delineating hydrothermal alterations related to UNYG, two spectral indices, including Kaolinite Index (KLI) = (b4/b5) *(b8/b6) and OH-bearing altered minerals index (OHI) = (b7/b6) * (b4/b6)), were applied and displayed in different RGB combinations to enhance their visibility (Ninomiya, 2003). To create color composites, KLI and OHI were calculated and displayed as KLI-b1-b3 and OHI-b4-b6 in RGB, respectively (Fig. 10). KLI and OHI show that altered minerals (bearing kaolinite and hydroxyl) such as kaolinite and muscovite exhibited high reflectance feature in SWIR bands 4, 7, and 8. The image of the indices indicates that hydrothermal alteration is well developed and invaded a considered part of the study area, represented by rose (KLI) and orange (OHI) colors, predominately over younger granites, and supports the differentiation of band ratio combinations. Moreover, the distribution patterns of alteration minerals extracted based on the indices correlate very well with the pattern extracted based on other processing techniques confirming the capacity of SIR to identify hydrothermal alteration minerals using ASTER data.

5.2. Machine learning results

Lithological classification results of ASTER, S2, and ASTER + S2 demonstrated the capability of the three datasets to achieve reasonable generalization utilizing SVM, however, several differences are highlighted. Fig. 11 shows the resultant three thematic maps for all thirteen lithological classes, including albitized granite, biotite alkali feldspar granite, ophiolitic metavolcanics, trachyte, acidic arc metavolcanics, older granite, serpentinite, basic to intermediate arc metavolcanics, metasedimentary rocks, metagabbro-diorites, alkali granite, wadi deposits, and hydrothermal alteration. These results were evaluated and compared using the confusion matrix's producer accuracy (PA), user accuracy (UA), overall accuracy (OA), and Kappa coefficient (K) (Table 5). The Kappa coefficient quantifies the level of concordance between the classified map and the reference data (Congalton, 1991; Kumar et al., 2020; Ray, 2019, Serbouti et al., 2021). The Kappa coefficient is distinct from the overall accuracy since it considers the complete contingency matrix and is intended to evaluate the consistency of the results.

The ASTER-derived thematic map demonstrated higher overall accuracy and kappa coefficient (86.6 % and 0.85, respectively) relative to S2 (79.5 % and 0.77, respectively). The superior results of ASTER-based classification over S2-based classification can be explained by the higher and narrower spectral resolution of the ASTER SWIR bands. These results confirm that ASTER effectively discriminates the lithological spectral information more accurately than S2, which still delivers a reasonable lithological mapping. In addition, utilizing the combined ASTER and S2 data is significantly superior to that based solely on ASTER or S2 data. Remarkably, applying SVM over ASTER + S2 datasets achieved the highest overall accuracy (91.2 %) and kappa coefficient (0.90). Besides the great coincidence with our field observations, and visual interpretations of the previous geological maps, this fusion-based classification has significantly improved the detailed producer and user

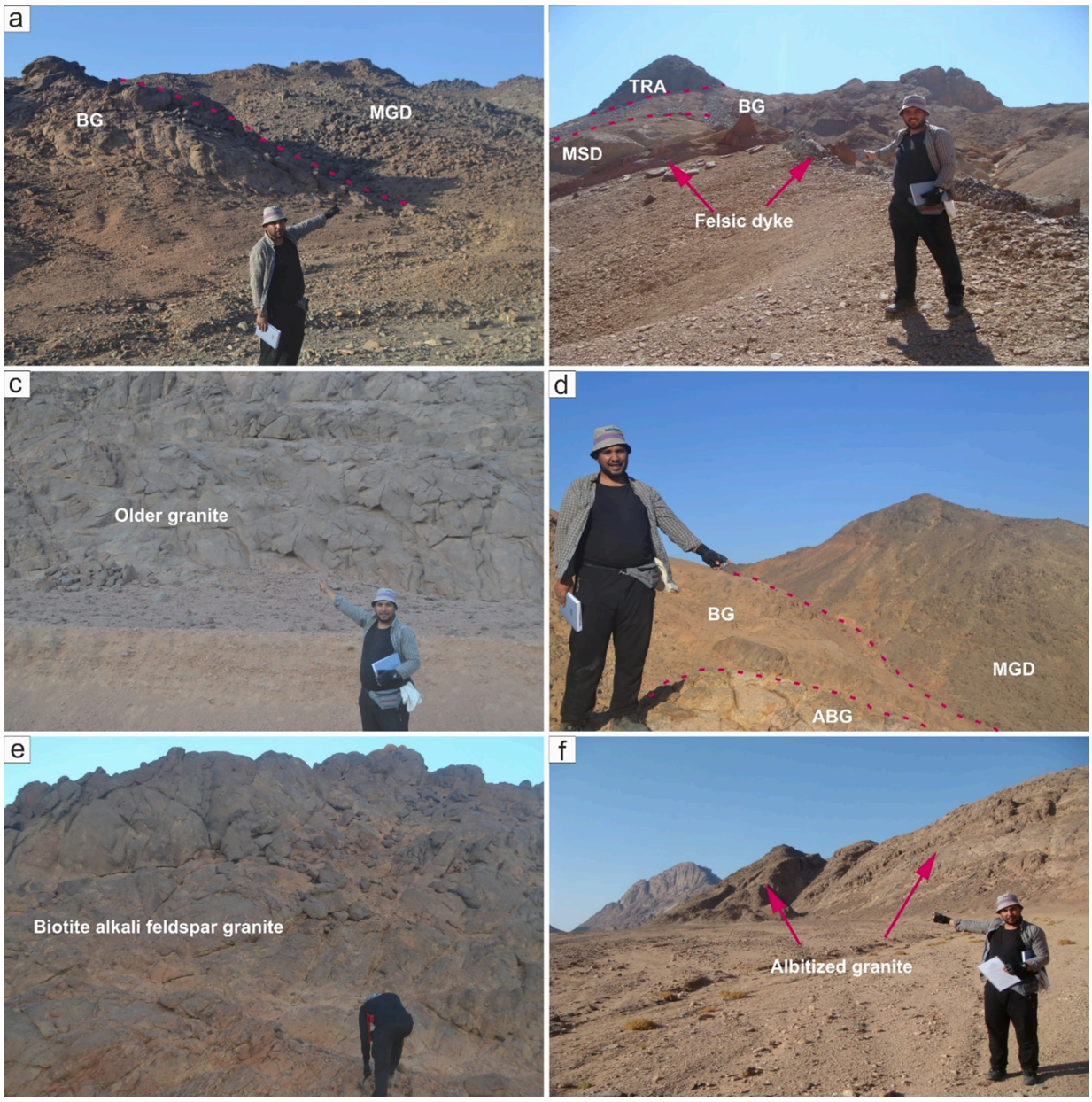

Fig. 14. Field photographs showing the mapped rock units and hydrothermal alteration zones of (a) the contact between biotite alkali feldspar granite (BG) and metagabbro-diorites (MGD), (b) Biotite alkali feldspar granite (BG) intruding in metasedimentary rocks (MSD) and trachyte (TRA) plugs on top, (c) outcrop of the mapped older granites in the study area, (d) Contacts between albitized granite, biotite alkali feldspar granite, and metagabbro-diorites in the southern part of UNYG, (e) outcrop of the mapped biotite alkali feldspar granite in the study area, and (d) Additional outcrop of the mapped, non-reported albitized granite in the southern part of the study area.

accuracies for the majority of classes. UA refers to how precisely classified points are real on the ground. For instance, the UA of albitized granite has increased from 87.79 % (AST-based) to 99.62 % (S2 and AST-based), as well as the UA of biotite alkali feldspar granite has increased from 95.29 % (S2-based) to 96.79 % (S2 and AST-based). The fusion-based classification demonstrates impressive higher OA accuracy since incorrectly-classified pixels using ASTER or S2, individually, were accurately classified utilizing the fused ASTER-S2 data. These analyses indicate that using high spectral resolution datasets provide better accuracy than using datasets with high spatial resolution; and that combining high spectral and spatial resolution datasets yielded superior classification results to using a single dataset. The benefit of fused AST-S2 classification is also clarified by the improved generalization of WD, despite their usual misclassification due to the abundance of different rock boulders in the low-topography area. Utilizing the stacked AST-S2 data for SVM classification improved the spectrometric data and, consequently, the classification OAs, where S2 and AST delivered significantly lower OAs of 79.5 % and 86.6 %, respectively than the higher OA of 91.2 % for the fused AST-S2 classification. Variations in OAs can primarily be attributed to the varying spectral and spatial resolutions of the datasets utilized in the SVM analysis. These differences in lithological discernability are statistically reflected by checking the UAs and PAs of the classified targets. For example, the combined AST-S2 classification improved the separation of lithological units exhibiting closer spectral characteristics (due to the similarity in mineralogical composition), such as varieties of granitic rocks and acidic metavolcanics. Differentiating these spectrally-related rock units using standard methods of remote sensing mapping is difficult. For example, four types of granitic rocks within the study area are reasonably discriminated (ABG, ALK, BG, OGR) with the application of AST-S2

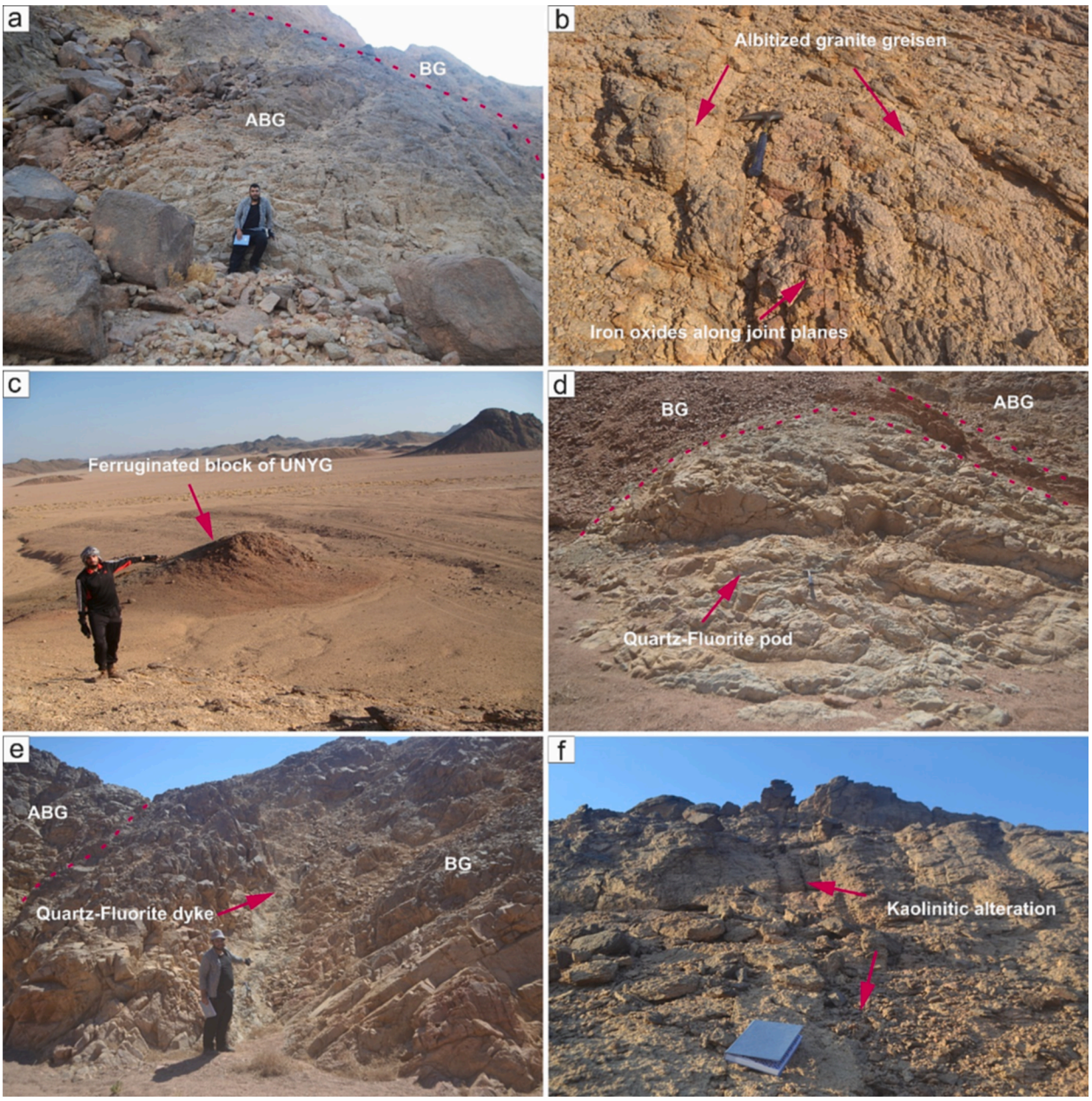

Fig. 15. Field photographs showing the mapped rock units and hydrothermal alteration zones of (a) a newly recorded outcrop of the albitized granite (ABG) in contact with biotite alkali feldspar granite (BG) in the eastern part of the study area, (b) albitized granite show greisen alteration with red iron oxides invading the joint planes, (c) a block of Umm Naggat younger granite (UNYG) has undergone extensive ferrugination, (d), (e) Fluorite-silica pod and vein occurring near the albitized granite, and (f) a block of younger granite extensively altered to kaolinite. (For interpretation of the references to color in this figure legend, the reader is referred to the web version of this article.)

allocation. The UAs of ABG, BG, OGR, and ALK have remarkably increased, from S2-based results of 70.57 %, 95.29 %, 77.72 %, and 75.15 % to AST-S2 UAs of 99.62 %, 96.79 %, 93.27 %, and 100 %, respectively. In addition, the PAs of the HYD class demonstrate a gradual classification improvement from S2 to AST and AST-S2 inputs, enhanced from 97.68 % to 99.23 % and 100 %, respectively. These results demonstrate the competence of the SVM classifier in separating the spectral signatures of various kinds of lithologies and surface alterations.

Besides these statistical accuracy analyses, a visual comparison of the three final thematic layers demonstrated that better visual lithological discrimination, in terms of homogeneity, elimination of erroneous pixels (decreasing salt and pepper effect), and accurate spatial classification of the mapped rock units is noticed with AST + S2 thematic map compared to that of AST or S2 individually (Fig. 11). In AST or S2 classification images (Fig. 11a, b), older granites are frequently misclassified as metavolcanics on the eastern and western sides of the Umm Naggat area. The UA of OG improved from 77.72 % (S2) to 93.27 % (AST-S2), resulting in a more precise allocation of pixels, making its borders more distinct and accurately delineated with nearby rock units, such as metavolcanics.

In addition, a statistical and spatial comparison of the outcomes of albitized granite, biotite alkali feldspar granite, alkali granite, and Trachyte in Table 5 and Fig. 11 demonstrates that AST-S2 integration improves categorization and mapping over their respective individual inputs. ABG was occasionally misclassified and misinterpreted as ALK in the northern portion of UNYG or as BG and TRA in the southern part due to their comparable mineralogical and chemical properties of

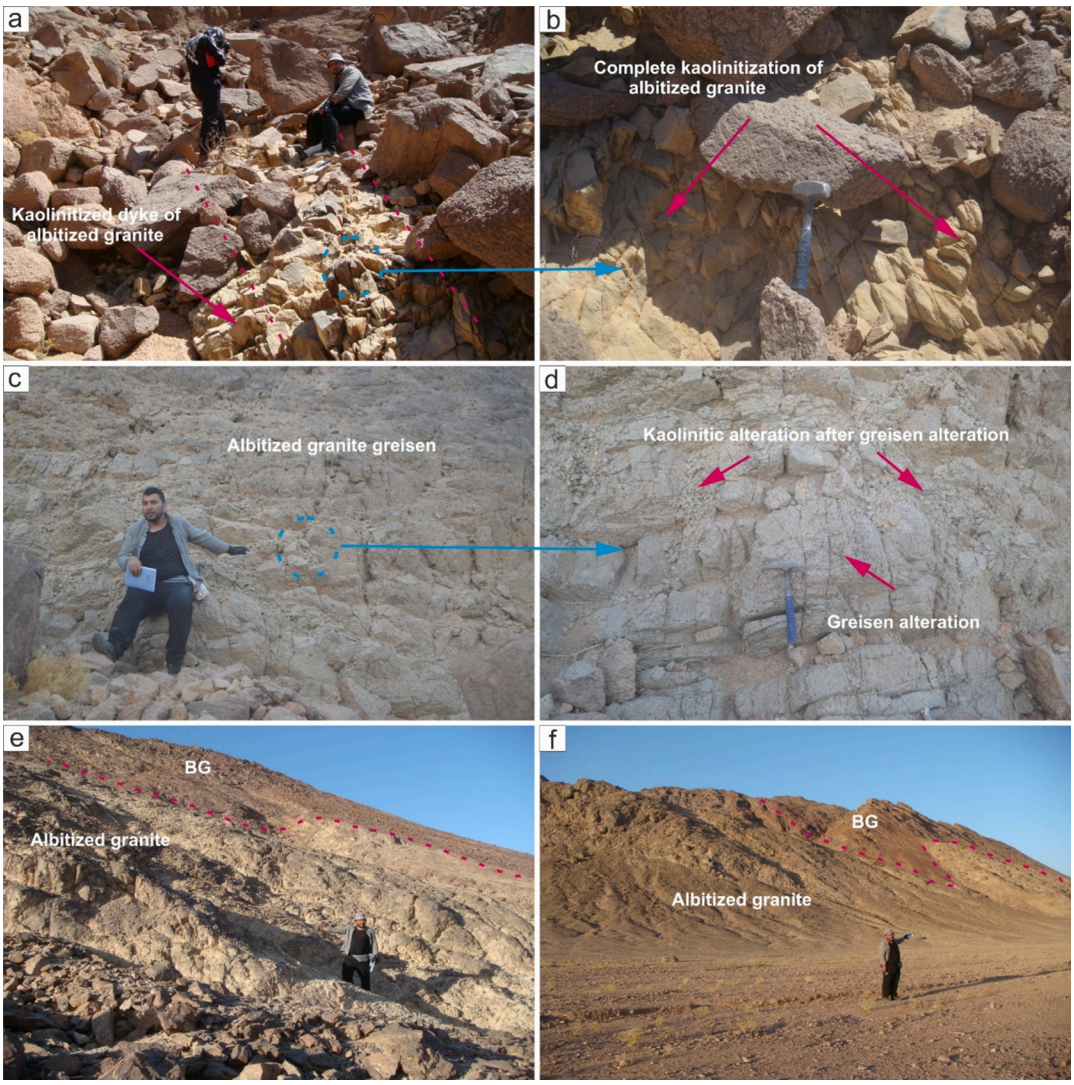

Fig. 16. Field photographs showing the mapped rock units and hydrothermal alteration zones of (a) a dyke of albitized granite completely altered to kaolinite, (b) a zoomed view from figure number 16a shows the kaolinitic alteration product (c) albitized granite showing extensive greisen alteration, (d) a zoomed view from Fig. 16c showing the kaolinitic alteration that followed greisen alteration, (e) and (f) a newly recorded outcrop of the albitized granite (ABG) in contact with biotite alkali feldspar granite (BG) in the southwestern part of the study area.

significant alkali feldspars (potassium and sodium) concentrations. Remarkably, AST-S2 blending has amplified the minute variations between ABG and the other classes resulting in good discrimination due to these mineralogical differences. As a result, not only was the UA of ABG increased from 70.57 % (S2) to 87.79 % (AST) and 99.62 % (AST-S2) but also the accuracies of TRA and ALK improved respectively from 63.16 % and 75.15 % (S2) to 100 % (AST-S2). This improved statistical correctness can be visualized and traced in the composite image (Fig. 11c), which generates classes that are more uniform, homogenous, and clearly defined. Closer to our target (ABG), the combined AST + S2 has significantly improved its lithological differentiation from the other rock units, particularly those with similar spectral signatures, and successfully delineated the spatial distribution (after verification through fieldwork) of mineralized units and hydrothermal alterations in the study area. Therefore, the AST + S2 SVM thematic map was adopted as a final lithological map for the study area, manifesting clearly defined lithological contacts and verified alteration zones (Fig. 12).

6. Discussion and geological validation

The integrated ASTER -S2 results were utilized for the first time in Umm Naggat area and proved their efficiency in precise lithological discrimination, as well as accurate detection of potentially mineralized albitized granite and its spatially-associated hydrothermal alteration. Fieldwork (field geology, field sampling, and field photos), as well as previous geological maps (Abd El Nabi, 2012; Al-Arifi et al., 2021; Badr et al., 2014; El–Afandy, Abdalla, 2000; Gaafar, 2015; Gaafar et al., 2022' Hassanen et al., 2008) were used to validate remote sensing and machine learning results (Fig. 13).

The comprehensive lithological mapping as felsic (granites and acidic metavolcanics) and mafic (serpentinites, basic metavolcanics, and ophiolitic metavolcanics) varieties, was executed from ASTER band ratios b4/b6-b8-b5 RGB (Fig. 6b, 14a, 14b). Likewise, the exposed arc and ophiolitic metavolcanics in the study area were separated using the ASTER SWIR-TIR band ratio composite of b8-b4-b9/b10 (Fig. 7a) (Table 1). Subsequently, S2 results (MNF1-MNF2-MNF3 in RGB) (Fig. 8c) discriminated OMV where the FCC of b12-b11-b2 in RGB successfully differentiated OGR as well as arc metavolcanics into acidic (AMV) and basic to intermediate (BMV) varieties (Fig. 4b). Consequently, most of the exposed rock units were precisely discriminated utilizing the former image processing techniques.

To ensure a more detailed differentiation for Umm Naggat granitic

Table 6
Summary of remote sensing results for used datasets and processing techniques.

Data	Technique	RGB	Rock Units	Color	Legend	Figure
ASTER	OIF	b1-b5-b9	UNYG	bluish violet		Fig. 3a
			AMV-OMV	dark green		
			OG-MSD-MGD-SP-BMV	reddish brown		
ASTER	FCC	b8-b5-b1	UNYG	yellowish Beige		Fig. 3b
			OG-MSD-MGD-SP	violet		
		b8-b4-b12	UNYG	golden violet		Fig. 3c
Sentinel-2	FCC	b12-b6-b2	UNYG	buff		Fig. 4a
			MV-OG	purple		
			MGD-SP-MSD	bluish-grey		
			TRA-HYD	green		
		b12-b11-b2	OG	fuchsia rose		Fig. 4b
			UNYG	yellowish brown		
			AMV	greenish brown		
			BMV	greenish purple		
			MSD	dark blue		
			MGD	greenish blue		
			SP	brownish green		
			HYD	green		
			Li-bearing	violet		
		b11-b12-b7	TRA- Li bearing	blue		Fig. 4c
			MGD	reddish brown		
			MSD	violet		
			SP	green		
			HYD	fuchsia		
ASTER	BR	b4-b6-b4/b5	MGD-SP	bluish violet		Fig. 6a
			Iron oxides	light violet		
		b4/b6-b8-b5	SP	dark green		Fig. 6b
			UNYG	light green		
			OG	crinkled dark green		
			AMV	blue		
			BMV	purple		
			OMV	bluish black		
		b8-b4-b1/b4	Li-bearing	bright violet		Fig. 6c
		b8-b4-b9/b10	AMV-BMV	deep green		Fig. 7a
			OMV	greenish black		
		b8-b4-b4/b6	HYD	Cyan		Fig. 7b
ASTER	RBD	b4-b8-RBD6	UNYG-OG	green		Fig. 7c
			HYD	light violet		
Sentinel-2	PCA+ICA	PCA1-PCA2-ICA2	ALK	pale red		Fig. 8a
			ABG+BG	green		
			TRA-HYD	deep red		
		ICA2-PCA3-PCA4	HYD	yellow		Fig. 8b
Sentinel-2	MNF+DS	MNF1-MNF2-MNF3	OMV	forest green		Fig. 8c
			HYD	red		
		MNF2-MNF3-MNF1	ABG	purple		Fig. 9a
			ALK	green		
			BG	light yellow		
			AMV	rose		
			MGD	blackish green		
		MNF2-MNF3-MNF4	HYD	blue		Fig. 9b
			ABG	purple		
			ALK	green		
			BG	yellow		
		DS3-MNF2-b11	MSD	deep red		Fig. 9c
			HYD	blue		
ASTER	SIR	KLI-b1-b3	HYD	rose		Fig. 10a
		OHI-b4-b6	HYD	orange		Fig. 10b

rocks (younger and older granites), several remote sensing techniques were successfully implemented for their lithological characterization, especially UNYG, which is recognized for its diverse rare metal resources (El-Qassas et al., 2021, Gaafar, 2015). Umm Naggat albitized granite has known metallogenetic importance due to significant quantities of tantalum and niobium (0.02 % Ta and 0.03–0.15 % Nb) (Abdalla et al., 1996, El–Afandy et al., 2000, Sabet rt al., 1976b) and other rare metals such as Sn, U, Zr, and REE, and is classified as rare metal granite (Abd-Elmeguid et al., 2003, Abd El Nabi, 2012, Al-Arifi et al., 2021, El-Qassas et al., 2021, El–Afandy et al., 2000, Gaafar, 2015, Gaafar and Ali, 2015). Thus, we implemented ASTER's six SWIR and five TIR bands (Table 1) for better lithological mapping of granitic rocks due to their effectiveness in detecting the absorption properties of phyllosilicates (Aboelkhair et al., 2010, Yamaguchi et al., 1998, Yamaguchi and Naito, 2003).

Primarily, the granitic rocks (UNYG and OGR) were identified using an ASTER SWIR color composite of b4-b8-RBD6 (Fig. 14c). UNYG with metavolcanics displayed the same color utilizing both SWIR-TIR FCC b8-b4-b12 in RGB. Moreover, the three FCCs of S2 b12-b6-b2, ASTER b8-b5-b1, and OIF b1-b5-b9 in RGB accurately demarcated the boundary between UNYG and the adjacent country rocks.

Based on our fieldwork, remote sensing results, and previous investigations (Al-Arifi et al., 2021, Badr et al., 2014, Gaafar, 2015), the UNYG could be subdivided into three distinct rock units: biotite alkali feldspar granite, alkali granite, and albitized granite (Fig. 14d). For instance, S2 transformations demonstrated the most remarkable capacity to differentiate the UNYG and isolate the mineralized albitized granite as the study's main concentration. The color composite of PCA1-PCA2-ICA2 in RGB distinguished the UNYG pluton principally into two

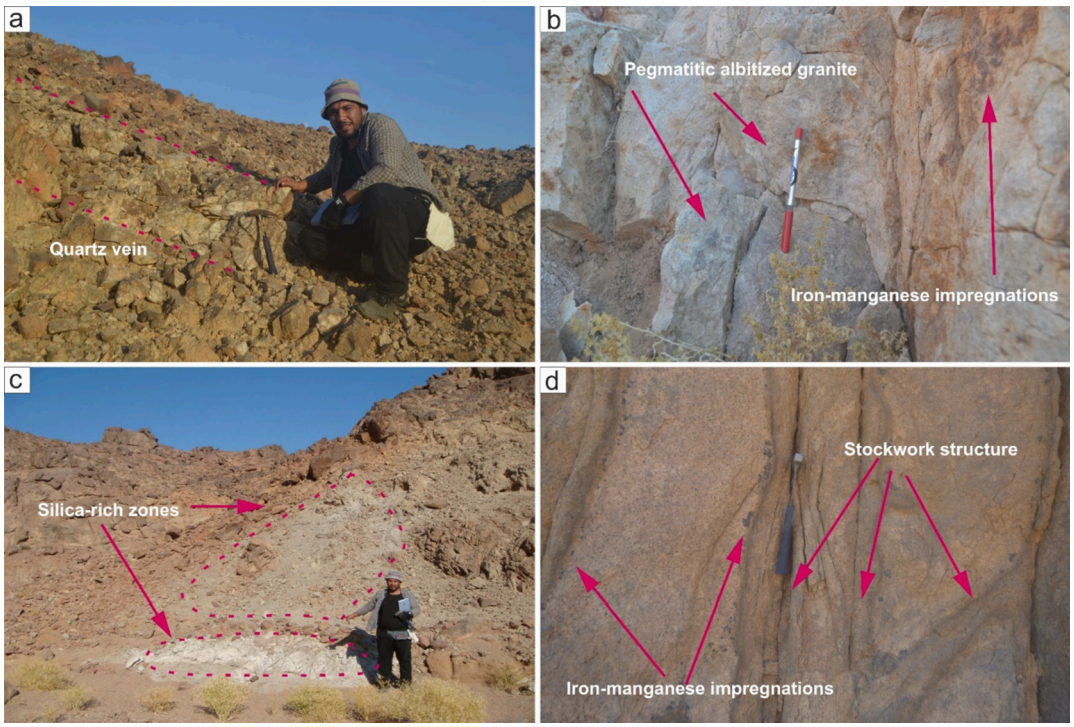

Fig. 17. Field photographs showing the mapped rock units and hydrothermal alteration zones of (a) a quartz vein cutting through younger granite in the study area, (b) a Pegmatitic albitized granite hosts staining of iron and manganese oxides, (c) two zones rich in silica occurring within younger granite in the study area, and (d) several impregnations of iron and manganese with stockwork structure occurring along joint planes within younger granite in the study area.

categories: albitized and biotite alkali feldspar granites (first category), as well as alkali granite (second category). More specification is introduced through the S2 MNF2-MNF3-MNF1 and MNF2-MNF3-MNF4 color composites in RGB, distinguishing biotite alkali feldspar granite, alkali granite, and albitized granite as three different units (Fig. 14e, 14f, 15a).

Subsequent to this detailed lithological identification of UNYG, special attention was given to detecting hydrothermal alterations such as iron-oxide, hydroxyl-bearing minerals, lithium-bearing minerals, fault-related hydrothermal alteration, and clay minerals using ASTER data. Iron oxides alteration minerals were differentiated and highlighted by utilizing ASTER b4-b6-b4/b5 (Fig. 6a, 15b, 15c). Similar to Mashkoor, Ahmadi (2022) results, Lithium-bearing minerals such as mica were effectively marked by using the ASTER band ratio b8-b4-b1/b4 in RGB (Fig. 6c). El–Afandy, Abdalla (2000) and Mohamed et al. (1999) documented both F and Li enrichment as well as the occurrence of Li-rich mica (siderophyllite) with replacing nature for feldspars in the albitized granite in the study area (Fig. 15d, 15e). Additionally, ASTER-based KLI and OHI were used to detect kaolinitic and hydroxyl-bearing alterations (Fig. 15f). Kaolinization usually follows other alteration processes and is revealed by partial to complete decomposition of feldspar and mica into clay minerals (Fig. 16a, 16b). Greisen alteration of UNYG was followed locally by argillic alteration (kaolinite and illite) of the granite greisen (owing to extended H + -metasomatism and acid leaching) (El–Afandy et al., 2000) (Fig. 16c, 16d). ASTER band ratio of b8-b4-b4/b6 and S2 transformations of ICA2-PCA3-PCA4, MNF1-MNF2-MNF3, and DS3-MNF2-b11 identified fault-related hydrothermal alterations (Fig. 7b, 8b, 8c, and 9c). All lithological discrimination and hydrothermal alteration mapping results are summarized in Table 6.

After comparing the current results with previous studies (Abd El Nabi, 2012, Al-Arifi et al., 2021, El-Qassas et al., 2021, El–Afandy et al., 2000, Gaafar, 2015, Gaafar and Ali, 2015) reporting that albitized granite (ABG) is exposed as dome-shaped protrusions or cupolas, only in the northern part of UNYG (as a body of nearly 0.6 km in width and 3 km in length), our remote sensing results and field investigations revealed new ABG occurrences at the southern and southwestern part of UNYG (Fig. 14f, 16e, 16f). These new occurrences are verified and interpreted in light of the well-known theories of albite-rich granite genesis. The origin of albite-rich granites in the African Nubian Shield is still under debate. Its genetic hypotheses include (1) metasomatic origin (Beus, 1968, Beus et al., 1962, El-Tabal, 1979, Riad, 1979, Sabet et al., 1976a), (2) magmatic origin (Abou El Maaty and Ali, 2000) and (3) a combination of metasomatic and magmatic origins (Azer et al., 2019, Mohamed, 2013, Moussa et al., 2021). Therefore, emphasizing the spatial relationship between hydrothermal alteration and structural developments in rare-metal albitized granite is crucial to our study.

During fieldwork verification, the newly reported occurrences of albitized granite (in the southern and southwestern parts of UNYG) (Figs. 14, 15, 16, 17)) are characterized by substantially altered zones occurring in different widths and lengths. Various alteration processes, including albitization, greisen alteration (Fig. 15b, 16b, 16c), kaolinization (Fig. 16a, b, d) and fluoritization (Fig. 15d) are associated with albitized granite, particularly along significant NW, NNW, NNE, and N-S trending faults, as well as fluorite (Fig. 15e) and quartz veins (Fig. 17a). Similar field features were previously reported in the northern albitized granite of the UNYG body by other researchers (Abd El Nabi, 2012, Al-Arifi et al., 2021, El-Qassas et al., 2021, El–Afandy et al., 2000, Gaafar, 2015, Gaafar and Ali, 2015). They indicated that the northern portion of the Umm Naggat granite pluton has undergone extensive post-magmatic metasomatic alteration, resulting in the formation of a Zr, Hf, Nb, Ta, U, Th, and F, and kaolinized, albite-enriched (Na-metasomatized) granite greisen. Furthermore, our field investigations revealed several occurrences of albitized pegmatite (Fig. 17b). The presence of rare-metal pegmatite mineralization on the periphery of albitized granites in the southwestern portion of UNYG shows that metasomatism might have played a key role in the mineralization process as reported in similar areas with rare metal albitized granite in the Eastern Desert (Azer et al., 2019, Moussa et al., 2021, Zoheir et al., 2020). Gaafar (2015) identified similar pegmatitic albitized sites in the northern ABG of UNYG and indicated that they are significantly enriched in niobium relative to tantalum and usually associated with fluorite. The former silica-rich

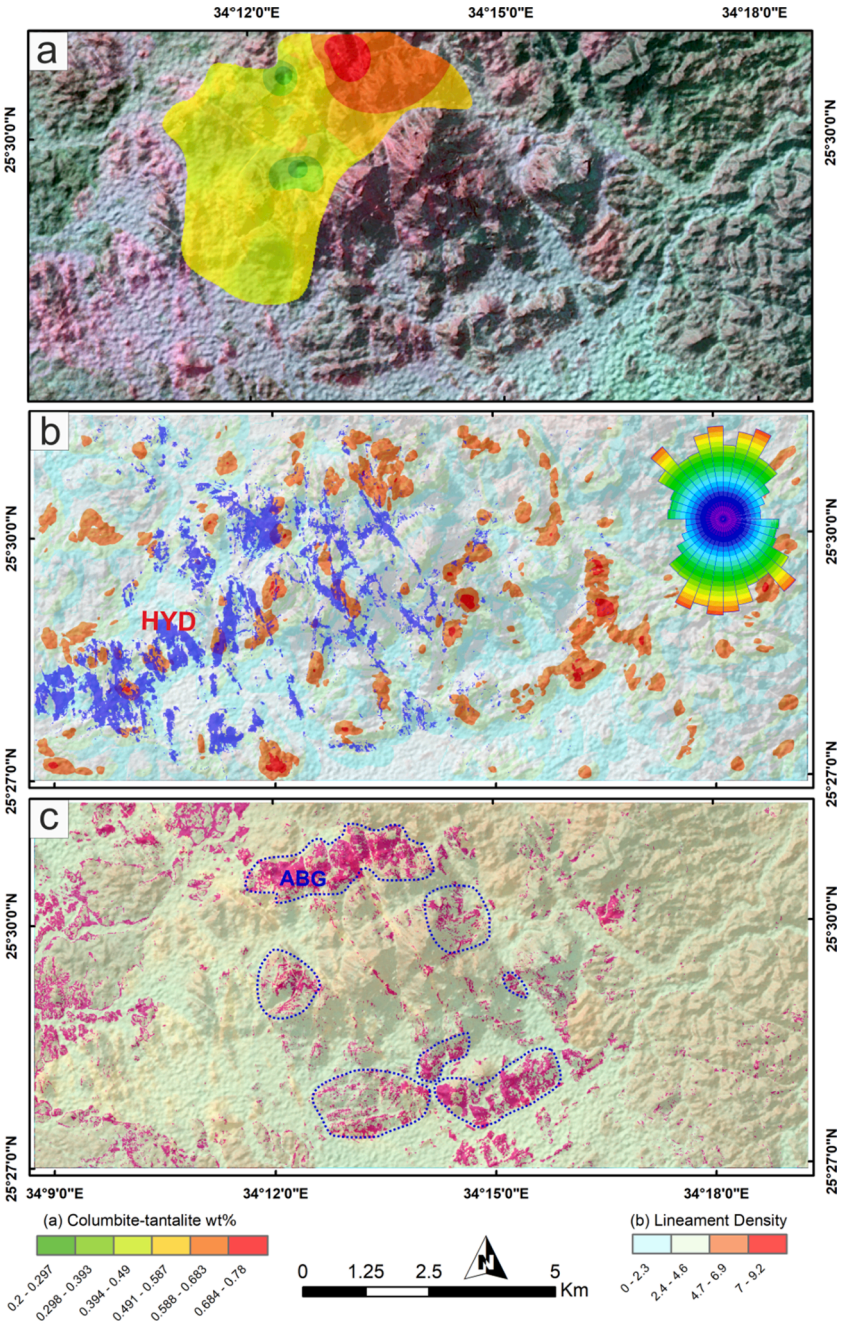

Fig. 18. Thematic maps verification using (a) Quantitative columbite-tantalite distribution in the northern part of the study area after Badr et al. (2014), (b) Integrated hydrothermal alteration zones, structural density map, and rose diagram demonstrating the spatial correlation between the predominant structural trends and their density with highly altered zones, and (c) Verified distribution of albitized granite in the study area (based on SVM classification results and fieldwork); proposed exploration targets are circled in blue color. (For interpretation of the references to color in this figure legend, the reader is referred to the web version of this article.)

pegmatites are commonly found close to alteration zones in the southwestern boundaries of UNYG (Fig. 17c). These associations were recorded in the northeastern part of UNYG around the peripheries of albitized granite (Gaafar and Ali, 2015).

Additionally, several impregnations of black Mn-oxide and red hematitic alterations, stockwork structures, as well as numerous shear zones were discovered close to the albitized granite in the southern regions of UNYG (Fig. 17c, 17d). El–Afandy, Abdalla (2000) discovered comparable alterations in the albitized granite north of UNYG and stated that these alterations concluded the albitization and greisen alteration processes and may be indicative of the fluids oxidized state. These Fe-Mn impregnations are usually recorded with several locations of rare-metals albitized granite in the central and southern Eastern Desert in Egypt (Abdalla et al., 1996, Abdalla et al., 1994, Abuamarah et al., 2021, Azer et al., 2019, Moussa et al., 2021, Zoheir et al., 2020). Numerous Fluorite -quartz pods and veins trend mainly in the N20W, N-50 W, and S40E directions were recorded (Fig. 15e, 17a). In previous studies, analogous fluoritization in the northern part of UNYG was indicated by the development of fluorite-rich granite greisen zones and fluorite pods (El–Afandy et al., 2000).

The hydrothermal alteration zones associated with albitized granite in the study area are also structurally controlled (Al-Arifi et al., 2021, Gaafar, 2014, 2015). Rare metals-bearing granites in the Central Eastern Desert of Egypt were emplaced in an extensional tectonic regime along inherited ductile fabrics (Azer et al., 2019, Gaafar and Ali, 2015, Helba et al., 1997). Umm Naggat structures are associated with the Eastern Desert (ED) major structures, such as the Arabian Nubian Shield (ANS) and the Najd fault zone (El-Qassas et al., 2021, Hamimi et al., 2015), where the majority of ED deposits were formed by fluid infiltration, superstructure deformation, and infrastructure magmatism (Stern, 2018).

Since the majority of mineral resources are affected directly or

indirectly by structures, structural lineament analysis plays a crucial role in mineral exploration (Ali et al., 2008, Eldosouky et al., 2017, Mahdi et al., 2022, Maleki et al., 2021, Sheikhrahimi et al., 2019, Tripathi et al., 2022). Field investigations and automatic lineament extraction demonstrated various regional structural trends oriented in the NW, NNW, NNE, and N-S (Fig. 18b). They are mainly classified as strike-slip faults of NW-SE and NNE-SSW trending, and The interaction between these two fault systems, which confine the albitized granite north of UNYG, is readily observable, indicating that these surface geological structures have subsurface extensions (Gaafar, 2015, Gaafar and Ali, 2015). Numerous felsic, fluorite, and quartz veins infiltrated the Um Naggat body in the NW–SE and N-S orientations. These structures play a significant role in mineral prospecting because they may host mineral-rich fluid conduits. According to Gaafar (2015) and Gaafar and Ali (2015), faults, fractures, and shear zones play the most significant role in Nb, Ta, and Sn mineralization in the Um Naggat region, where they host the majority of the rare metal deposits; the continuous reactivations of these structures have a tremendous impact on both the distribution and mode of mineralization.

The integration of SVM classification of stacked AST-S2 bands, remote sensing findings, lineament density map, fieldwork, and prior studies, was successful in not only producing an accurately-discriminated lithological map but also identifying the new occurrences of albitized granite and their associated alterations of the Um Naggat pluton as a potentially mineralized zones (Fig. 18). These zones are distinguished by abundant rare metal mineralization, which is dominated by several types of related hydrothermal alteration and four major structural trends in the NW, NNW, NNE, and N-S. The results demonstrated a close correlation between albitized granite, hydrothermal alteration patterns, and structural controls.

Quantitative columbite-tantalite distribution in the northern part of UNYG, demonstrating verified mineralization locations, is documented by Badr et al. (2014) and confirmed by other studies (Al-Arifi et al., 2021, Gaafar, 2015). These locations (with given concentrations as shown in Fig. 18a) are mostly the same zones suggested by the current study revealing the advantageous spatial correlation between the structural lineaments, hydrothermal alteration zones, and albitized granite in highlighting rare metal mineralization potential zones in the Umm Naggat region. Besides confirming the known mineralized locations, our results revealed some new potential zones, especially in the southern and southwestern parts of the study area. Moreover, the integrated hydrothermal zones-structural density map demonstrates that the predominant structural trends in alteration zones are NW, NNW, NNE, and N-S, indicating a possible fluid movement along these directions (Fig. 18b). The resulting distribution of the albitized granite demonstrated that the hydrothermal system is generally dominated by structural controls and is spatially related to the occurrences of albitized granites. This triple matching (alteration-structure-albitized granite) sheds light on additional favorable locations for potential rare metal deposits in the study area.

These results are introduced through a reconstructed geological map recording the new occurrences of rare-metals albitized granite (mainly in the southern and southwestern parts of the study area) (Fig. 12 and Fig. 18c). Furthermore, our outputs indicate a regional concordance between mineralized albitized granite, structural lineaments and alteration zones should be famed in future research as several locations of the previously reported mineralization occurrences coincided with the extracted albitized granite, hydrothermal alteration, and structural lineaments.

7. Conclusion

Our study integrates eight different image processing techniques and a machine learning algorithm (SVM) for the efficient interpretation of S2 and ASTER data in order to define albite-altered granite outcrops and associated rare-metal mineralization in the Umm Naggat area, Central Eastern Desert, Egypt. The results culminate in a geological interpretation map including hydrothermal alteration zones, structures and lithological boundaries, verified by detailed field observations, and allow us to draw the following conclusions:

The integration of several different image processing techniques in the interpretation of spectral remote sensing data (ASTER-S2) enabled us to effectively distinguish between different lithologies and hydrothermal alteration assemblages. Our interpretation map was used for the training and testing of the support vector machine algorithm (SVM).

Combined ASTER-S2 data is an efficient input (compared to using ASTER or S2 data in isolation) for SVM in the delineation of different lithological units during an initial geological interpretation of the respective study area..

Several types of hydrothermal alteration (albitization, greisen alteration, kaolinization, fluoritization, OH-bearing minerals) related to rare-metals mineralization are accurately detected and spatially correlated with albitized granites.

The spatial association between NW-, NNW-, NNE- and *N*-trending structures, hydrothermal alteration zones and mineralized and albitized granite outcrops suggests that the rare-metal mineralization is mainly structurally-controlled..

Spatially-associated hydrothermal alteration zones, high-density structural zones, and albitized granite occurrences are proposed exploration targets for rare-metals mineralization (e.g., Ta-Nb-Sn).

Our study reveals additional outcrops of potentially mineralized albitized granites that were validated in the field, and are situated in the southern and southwestern parts of the study area. Future research will focus on the detailed mineralogical and geochemical documentation of the rare-metal mineralization, particularly where hosted by albite-altered granite intrusions..

Our results at Umm Naggat, Central Eastern Desert, Egypt, strongly encourage the integration of different image processing methods, as well as the use of support vector machine algorithm (SVM) techniques in the efficient remote sensing interpretation of albite-altered and rare metal-mineralized granite outcrops. Our study may serve as a template for rare-metal exploration in similar arid environments worldwide.

Declaration of Competing Interest

The authors declare that they have no known competing financial interests or personal relationships that could have appeared to influence the work reported in this paper.

Data availability

Data will be made available on request.

Acknowledgments

This study is a part of the first author's Ph.D. dissertation at Akita University. The authors are thankful to U.S. NASA and ESA for providing the data. The authors also greatly appreciate editors' and reviewers' valuable and profound comments. The authors deeply thank Prof. McIntosh Richard and Keith Kiama for their efforts in the English revision of the manuscript. Thanks to The Ministry of Education, Culture, Sports, Science, and Technology (MEXT) for supporting Mohamed A. Abdelkader as a Ph.D. scholar in the fiscal years 2022-2025 at Akita University in Japan. Thanks to the ministry of higher education and scientific research of Egypt. Ali Shebl is funded by the Stipendium Hungaricum scholarship under the joint executive program between Hungary and Egypt.

References

Abd El Nabi, S.H., 2012. An analysis of airborne gamma ray spectrometric data of Gabal umm Naggat granitic pluton, Central Eastern Desert, Egypt. JAKU: Earth Sci. 23, 19–42.

Abd El-Wahed, M., Kamh, S., Ashmawy, M., Shebl, A., 2019. Transpressive structures in the Ghadir Shear Belt, Eastern Desert, Egypt: evidence for partitioning of oblique convergence in the Arabian-Nubian Shield during Gondwana Agglutination. Acta Geol. Sin.-English Ed. 93, 1614–1646.

Abdalla, H., Matsueda, H., Ishihara, S., Miura, H., 1994. Mineral chemistry of albite-enriched granitoids at Um Ara, Southeastern Desert, Egypt. Int. Geol. Rev. 36, 1067–1077.

Abdalla, H., Ishihara, S., Matsueda, H., Monem, A.A., 1996. On the albite-enriched granitoids at Um Ara area, Southeastern Desert, Egypt. 1. Geochemical, ore potentiality and fluid inclusion studies. J. Geochem. Explor. 57, 127–138.

Abdeen, M.M., Allison, T., Abdelsalam, M.G., Stern, R.J., 2001. Application of ASTER band-ratio images for geological mapping in arid regions; the Neoproterozoic Allaqi Suture, Egypt. Abstract Program Geol. Soc. Am. 3, 289.

Abd-Elmeguid, A.A., Ammar, S.E., Ibrahim, T.M.M., Ali, K.G., Shahin, H.A., Omar, S.A., et al., 2003. Uranium potential of Eastern Desert granites, Egypt. Internal Report, (Unpublished) Nuclear Materials Authority, Egypt.

Aboelkhair, H., Ninomiya, Y., Watanabe, Y., Sato, I., 2010. Processing and interpretation of ASTER TIR data for mapping of rare-metal-enriched albite granitoids in the Central Eastern Desert of Egypt. J. Afr. Earth Sc. 58, 141–151.

Abou El Maaty, M., Ali, B.M., 2000. Petrology of alkali feldspar granites of Nuweibi and Gebel El-Mueilha, central Eastern Desert, Egypt. Egypt J. Geol. 44, 127–148.

Abou El-Magd, I., Mohy, H., Basta, F., 2015. Application of remote sensing for gold exploration in the Fawakhir area, Central Eastern Desert of Egypt. Arab. J. Geosci. 8, 3523–3536.

Abrams, M., Hook, S.J., 1995. Simulated ASTER data for geologic studies. IEEE Trans. Geosci. Remote Sens. 33, 692–699.

Abrams, M., Yamaguchi, Y., 2019. Twenty years of ASTER contributions to lithologic mapping and mineral exploration. Remote Sensing. 11, 1394.

Abuamarah, B.A., Azer, M.K., Asimow, P.D., Ghrefat, H., Mubarak, H.S., 2021. Geochemistry and petrogenesis of late Ediacaran rare-metal albite granites of the Arabian-Nubian Shield. Acta Geol. Sin.-English Ed. 95, 459–480.

Agrawal, N., Govil, H., Chatterjee, S., Mishra, G., Mukherjee, S., 2022. Evaluation of machine learning techniques with AVIRIS-NG dataset in the identification and mapping of minerals. Adv. Space Res.

Ahmed, A.H., 2022. Mineral Deposits and Occurrences in the Arabian-Nubian Shield. Springer Nature.

Akaad, M., Noweir, A., 1978. Geology and lithostratigraphy of the Arabian Desert orogenic belt of Egypt between latitudes25°35′ and 26°35′N. In: Cooray, P.G., Tahoun, S.A. (Eds.), Evolution and mineralization of the Arabian-Nubian Shield Inst Appl Geol Jeddah Bull. Pergamon, Oxford, pp. 127–135.

Al-Arifi, N., El-Din, G.K., Abdelkareem, M., Abdalla, F., 2021. Integration of remote-sensing, structural, and geochemical data for characterizing granitoid rocks in Um Naggat pluton, Central Eastern Desert, Egypt. Arab. J. Geosci. 14, 1–22.

Ali, K.G., Gaafar, I., Ibrahim, T., 2008. Structural control and geophysical signature of Kab Amiri Epi syenitized muscovite granite and associated uranium showings, central Eastern Desert, Egypt. Ann. Geol. Survey Egypt. 30, 21–41.

Ali-Bik, M.W., Hassan, S.M., 2022. Remote sensing-based mapping of the Wadi Sa'al-Wadi Zaghara basement rocks, southern Sinai, Egypt. Egypt. J. Remote Sens. Space Sci. 25, 593–607.

Ali-Bik, M.W., Gabr, S.S., Hassan, S.M., 2022a. Spectral characteristics, petrography and opaque mineralogy of the Oligo-Miocene basalts at Wadi Abu Qada-Wadi Wata area, west-central Sinai, Egypt. Egypt. J. Remote Sens. Space Sci. 25, 529–540.

Ali-Bik, M.W., Sadek, M.F., Hassan, S.M., 2022b. Basement rocks around the eastern sector of Baranis-Aswan road, Egypt: Remote sensing data analysis and petrology. Egypt. J. Remote Sens. Space Sci. 25, 113–124.

Amer, R., Kusky, T., El Mezayen, A., 2012. Remote sensing detection of gold related alteration zones in Um Rus area, Central Eastern Desert of Egypt. Adv. Space Res. 49, 121–134.

Asran, A.M., Emam, A., El-Fakharani, A., 2017. Geology, structure, geochemistry and ASTER-based mapping of Neoproterozoic Gebel El-Delihimmi granites, Central Eastern Desert of Egypt. Lithos 282, 358–372.

Assiri, A.M., 2016. Remote sensing applications for carbonatite assessment and mapping using VNIR and SWIR bands at Aluyaynah. Michigan State University, UA E.

Azer, M.K., Abdelfadil, K.M., Ramadan, A.A., 2019. Geochemistry and petrogenesis of Late Ediacaran rare-metal albite granite of the Nubian Shield: Case study of Nuweibi intrusion, Eastern Desert, Egypt. J. Geol. 127, 665–689.

Bachri, I., Hakdaoui, M., Raji, M., Teodoro, A.C., Benbouziane, A., 2019. Machine learning algorithms for automatic lithological mapping using remote sensing data: A case study from Souk Arbaa Sahel, Sidi Ifni Inlier, Western Anti-Atlas, Morocco. ISPRS Int. J. Geo-Inf. 8, 248.

Bachri, I., Hakdaoui, M., Raji, M., Benbouziane, A., Mhamdi, H.S., 2022. Identification of Lithology Using Sentinel-2A Through an Ensemble of Machine Learning Algorithms. Int. J. Appl. Geospatial Res. (IJAGR). 13, 1–17.

Badr, Y.S., Dawoud, M., Arab, A.A., 2014. Geochemical Prospecting for Radioactive Mineralization at G. Um Naggat-G. Atawy Area, Central Eastern Desert, Egypt. MSc Thesis. Menoufia Univ., Egypt;.

Bedell, R., 2001. Geological mapping with ASTER satellite: new global satellite data that is a significant leap in remote sensing geologic and alteration mapping. Special Publ., Geo. Soc. Nevada. 33, 329–334.

Bentahar, I., Raji, M., 2021. Comparison of Landsat OLI, ASTER, and Sentinel 2A data in lithological mapping: a case study of rich area (Central High Atlas, Morocco). Adv. Space Res. 67, 945–963.

Berg, M., Bondesson, E., Low, S.Y., Nordholm, S., Claesson, I., 2005. A combined on-line PCA-ICA algorithm for blind source separation. In: 2005 Asia-Pacific Conference on Communications. IEEE, pp. 969–972.

Bertoldi, L., Massironi, M., Visonà, D., Carosi, R., Montomoli, C., Gubert, F., et al., 2011. Mapping the Buraburi granite in the Himalaya of Western Nepal: remote sensing analysis in a collisional belt with vegetation cover and extreme variation of topography. Remote Sens. Environ. 115, 1129–1144.

Beus, A., 1968. Geochemical exploration for endogenic deposits of rare elements on the example of tantalum, Nedra. English translation, GSC Library, Ottawa, Moscow.

Beus, A., Severov, E., Sitnin, A., Subbotin, K., 1962. Albitized and greisenized granites (apogranites). Izdat Akad Nauk SSSR, Moscow.

Bishta, A.Z., Sonbul, A.R., 2021. Rock unit discriminations using image processing technique of Ablah area, Arabian shield, Saudi Arabia. J. Indian Soc. Remote Sens. 49, 1965–1984.

Campbell, J.B., Wynne, R.H., 2011. Introduction to remote sensing. Guilford Press.

Cardoso, J.-F., 1998. Blind signal separation: statistical principles. Proc. IEEE. 86, 2009–2025.

Cardoso-Fernandes, J., Teodoro, A.C., Lima, A., 2019. Remote sensing data in lithium (Li) exploration: A new approach for the detection of Li-bearing pegmatites. Int. J. Appl. Earth Obs. Geoinf. 76, 10–25.

Cardoso-Fernandes, J., Teodoro, A.C., Lima, A., Perrotta, M., Roda-Robles, E., 2020a. Detecting Lithium (Li) mineralizations from space: Current research and future perspectives. Appl. Sci. 10, 1785.

Cardoso-Fernandes, J., Teodoro, A.C., Lima, A., Roda-Robles, E., 2020b. Semi-automatization of support vector machines to map lithium (Li) bearing pegmatites. Remote Sens. 12, 2319.

Chavez, P., Berlin, G.L., Sowers, L.B., 1982. Statistical method for selecting Landsat MSS ratios. J. Appl. Photogr. Eng. 8 (1), 23–30.

Chavez, J.P., 1984. Image Processing techniques for Thermatic Mapper data. Proceedings, ASPRS-ACSM Technical Papers. 2:728-42..

Chen, C.H., Zhang, X., 1999. Independent component analysis for remote sensing study. Image and Signal Processing for Remote Sensing V. SPIE, pp. 150–158.

Chen, Q., Zhao, Z.-F., Xia, J.-S., Zhao, X., Yang, H.-Y., Zhang, X.-L., 2022. Improving the accuracy of hydrothermal alteration mapping based on image fusion of ASTER and Sentinel-2A data: a case study of Pulang Cu deposit, southwest China. Geocarto Int. 1–20.

Congalton, R.G., 1991. A review of assessing the accuracy of classifications of remotely sensed data. Remote Sens. Environ. 37, 35–46.

Cooper, G., 2003. Feature detection using sun shading. Comput. Geosci. 29, 941–948.

Cortes, C., Vapnik, V., 1995. Support-vector networks. Mach. Learn. 20, 273–297.

Costa, I.S.L., Tavares, F.M., de Oliveira, J.K.M., 2019. Predictive lithological mapping through machine learning methods: a case study in the Cinzento Lineament, Carajás Province, Brazil. J. Geol. Survey Brazil. 2, 26–36.

Cracknell, M.J., Reading, A.M., 2014. Geological mapping using remote sensing data: A comparison of five machine learning algorithms, their response to variations in the spatial distribution of training data and the use of explicit spatial information. Comput. Geosci. 63, 22–33.

Crosta, A., De Souza, F.C., Azevedo, F., Brodie, C., 2003. Targeting key alteration minerals in epithermal deposits in Patagonia, Argentina, using ASTER imagery and principal component analysis. Int. J. Remote Sens. 24, 4233–4240.

Crowley, J.K., Brickey, D.W., Rowan, L.C., 1989. Airborne imaging spectrometer data of the Ruby Mountains, Montana: mineral discrimination using relative absorption band-depth images. Remote Sens. Environ. 29, 121–134.

Dawoud, M., Abdel Ghani, I., Elsaid, M., Badr, Y., 2017. The integration of ASTER imagery and airborne gamma-ray spectrometry in lithological discrimination of Ras Barud-Um Tagher Area, North Eastern Desert, Egypt. Inter. J. Innov. Sci., Eng. Technol. 4, 9–23.

De Boissieu, F., Sevin, B., Cudahy, T., Mangeas, M., Chevrel, S., Ong, C., et al., 2018. Regolith-geology mapping with support vector machine: A case study over weathered Ni-bearing peridotites, New Caledonia. Int. J. Appl. Earth Obs. Geoinf. 64, 377–385.

Ding, C., Liu, X., Liu, W., Liu, M., Li, Y., 2014. Mafic–ultramafic and quartz-rich rock indices deduced from ASTER thermal infrared data using a linear approximation to the Planck function. Ore Geol. Rev. 60, 161–173.

Drusch, M., Del Bello, U., Carlier, S., Colin, O., Fernandez, V., Gascon, F., et al., 2012. Sentinel-2: ESA's optical high-resolution mission for GMES operational services. Remote Sens. Environ. 120, 25–36.

El Fels, A.E.A., El Ghorfi, M., 2022. Using remote sensing data for geological mapping in semi-arid environment: a machine learning approach. Earth Sci. Inf. 15, 485–496.

El Kati, I., Nakhcha, C., El Bakhchouch, O., Tabyaoui, H., 2018. Application of Aster and Sentinel-2A Images for geological mapping in arid regions: The Safsafate Area in the Neogen Guercif basin, Northern Morocco. Int. J. Adv. Remote Sens. GIS. 7, 2782–2792.

El Ramly, M., 1972. A new geological map for the basement rocks in the Eastern and Southwestern Deserts of Egypt. Ann. Geol. Surv. Egypt 2, 1–18.

El Shazly E. On the classification of the Pre-Cambrian and other rocks of magmatic affiliation in Egypt, UAR. International geological congress 22 1964.

El–Afandy, A.H., Abdalla, H.M., Aly, M.M., Ammar, F., 2000. Geochemistry and radioactive potentiality of Um Naggat apogranite, central eastern desert, Egypt. Resour. Geol. 50, 39–51.

Eldosouky, A.M., Abdelkareem, M., Elkhateeb, S.O., 2017. Integration of remote sensing and aeromagnetic data for mapping structural features and hydrothermal alteration

zones in Wadi Allaqi area, South Eastern Desert of Egypt. J. Afr. Earth Sc. 130, 28–37.
El-Gaby, S., El-Nady, O., Khudeir, A., 1984. Tectonic evolution of the basement complex in the Central Eastern Desert of Egypt. Geol. Rundsch. 73, 1019–1036.
El-Gaby, S., List, F., Tehrani, R., 1988. Geology, evolution and metallogenesis of the Pan-African Belt in Egypt. in: S. El-Gaby, S., RD Greiling, RD, (eds.). The Pan-African Belt of the North East Africa and Adjacent Areas. Vieweg Verlag, Wiesbaden.
El-Qassas, R.A., Ahmed, S.B., Abd-ElSalam, H.F., Abu-Donia, A.M., 2021. Integrating of Remote Sensing and Airborne Magnetic Data to Outline the Geologic Structural Lineaments That Controlled Mineralization Deposits for the Area around Gabal El-Niteishat, Central Eastern Desert, Egypt. Geomaterials. 11, 1–21.
El-Tabal, H., 1979. Mineralogical studies on some rare metal apogranites from Nuweibi and Abu Dabbab areas, Eastern Desert, Egypt. Al-Azhar University, Cairo, pp. 1–112. Master thesis.
Ewais, M., El Zalaky, M., Selim, A., Sharib, A.A., 2022. Implementation of ASTER data for lithologic and alteration zones mapping: Derhib area, Southern Eastern Desert, Egypt. J. Afr. Earth Sci., 104725
Fal, S., Maanan, M., Baidder, L., Rhinane, H., 2019. The contribution of Sentinel-2 satellite images for geological mapping in the south of Tafilalet basin (Eastern Anti-Atlas, Morocco). Int. Arch. Photogram., Remote Sens. Spatial Inf. Sci. 42, 75–82.
Frutuoso, R., Lima, A., Teodoro, A.C., 2021. Application of remote sensing data in gold exploration: Targeting hydrothermal alteration using Landsat 8 imagery in northern Portugal. Arab. J. Geosci. 14, 1–18.
Gaafar, I., 2014. Geophysical mapping, geochemical evidence and mineralogy for Nuweibi rare metal albite granite, Eastern Desert, Egypt. Open J. Geol.
Gaafar, I., 2015. Integration of geophysical and geological data for delimitation of mineralized zones in Um Naggat area, Central Eastern Desert, Egypt. NRIAG J. Astronomy Geophys. 4, 86–99.
Gaafar, M., Ali, K.G., 2015. Geophysical and geochemical signature of rare metal granites, Central Eastern Desert, Egypt: implications for tectonic environment. Al-Azhar Bull. Sci. 26, 15–32.
Gaafar, I., Elbarbary, M., Sayyed, M., Sulieman, A., Tamam, N., Khandaker, M.U., et al., 2022. Assessment of Radioactive Materials in Albite Granites from Abu Rusheid and Um Naggat, Central Eastern Desert, Egypt. Minerals. 12, 120.
Gabr, S.S., Hassan, S.M., Sadek, M.F., 2015. Prospecting for new gold-bearing alteration zones at El-Hoteib area, South Eastern Desert, Egypt, using remote sensing data analysis. Ore Geol. Rev. 71, 1–13.
Gabr, S.S., Hassan, S.M., Sadek, M.F., 2021. Application of Remote Sensing in Detecting Mineralized Zones in the Pan-African Belt of Egypt. The Geology of the Egyptian Nubian Shield. Springer, pp. 645–664.
Gad, S., Kusky, T., 2006. Lithological mapping in the Eastern Desert of Egypt, the Barramiya area, using Landsat thematic mapper (TM). J. Afr. Earth Sc. 44, 196–202.
Gad, S., Kusky, T., 2007. ASTER spectral ratioing for lithological mapping in the Arabian-Nubian shield, the Neoproterozoic Wadi Kid area, Sinai, Egypt. Gondwana Res. 11, 326–335.
Govil, H., Gill, N., Rajendran, S., Santosh, M., Kumar, S., 2018. Identification of new base metal mineralization in Kumaon Himalaya, India, using hyperspectral remote sensing and hydrothermal alteration. Ore Geol. Rev. 92, 271–283.
Green, A.A., Berman, M., Switzer, P., Craig, M.D., 1988. A transformation for ordering multispectral data in terms of image quality with implications for noise removal. IEEE Trans. Geosci. Remote Sens. 26, 65–74.
Guha, A., Mondal, S., Chatterjee, S., Kumar, K.V., 2022. Airborne imaging spectroscopy of igneous layered complex and their mapping using different spectral enhancement conjugated support vector machine models. Geocarto Int. 37, 349–365.
Hamimi, Z., El-Barkooky, A., Martines Frias, J., Fritz, H., Abd, E.-R., 2020a. The Geology of Egypt. Springer Nature Switzerland, p. 710.
Hamimi, Z., Zoheir, B., Younis, M., 2015. Polyphase deformation history of the Eastern Desert tectonic terrane in northeastern Africa. in: XII international conference “new ideas in earth sciences”, Muscow.
Hamimi, Z., Hagag, W., Kamh, S., El-Araby, A., 2020b. Application of remote-sensing techniques in geological and structural mapping of Atalla Shear Zone and Environs, Central Eastern Desert, Egypt. Arab. J. Geosci. 13, 1–27.
Han, W., Li, J., Wang, S., Zhang, X., Dong, Y., Fan, R., et al., 2022a. Geological Remote Sensing Interpretation Using Deep Learning Feature and An Adaptive Multi-source Data Fusion Network. IEEE Trans. Geosci. Remote Sens.
Han, W., Li, J., Wang, S., Zhang, X., Dong, Y., Fan, R., et al., 2022b. Geological Remote Sensing Interpretation Using Deep Learning Feature and an Adaptive Multisource Data Fusion Network. IEEE Trans. Geosci. Remote Sens. 60, 1–14.
Harvey, A., Fotopoulos, G., 2016. Geological mapping using machine learning algorithms. Int. Arch. Photogram., Remote Sens. Spatial Inf. Sci. 41.
Hassan, M., Hashad, A., 1990. Precambrian of Egypt. in: Said, R. (ed.) The geology of Egypt Balkema, Rotterdam, pp 201–248.
Hassan, S., Ramadan, T., 2015. Mapping of the late Neoproterozoic Basement rocks and detection of the gold-bearing alteration zones at Abu Marawat-Semna area, Eastern Desert, Egypt using remote sensing data. Arab. J. Geosci. 8, 4641–4656.
Hassan, S.M., Sadek, M.F., Greiling, R.O., 2015. Spectral analyses of basement rocks in El-Sibai-Umm Shaddad area, Central Eastern Desert, Egypt, using ASTER thermal infrared data. Arab. J. Geosci. 8, 6853–6865.
Hassan, S.M., Sadek, M.F., 2017. Geological mapping and spectral based classification of basement rocks using remote sensing data analysis: The Korbiai-Gerf nappe complex, South Eastern Desert, Egypt. J. Afr. Earth Sci. 134, 404–418.
Hassan, S.M., Youssef, M.A., Gabr, S.S., Sadek, M.F., 2022. Radioactive mineralization detection using remote sensing and airborne gamma-ray spectrometry at Wadi Al-Miyah area, Central Eastern Desert, Egypt. Egypt. J. Remote Sens. Space Sci. 25, 37–53.
Hassanen, M., Moghazi, A., Hashad, M., ElSayed, M., 2008. The role of crystal/melt and fluid fractionation in the genesis of Late Neoproterozoic rare metal-bearing A-type granite of Um Naggat pluton, Eastern Desert, Egypt. Egypt. Mineral.
He, L., Lyu, P., He, Z., Zhou, J., Hui, B., Ye, Y., et al., 2022. Identification of Radioactive Mineralized Lithology and Mineral Prospectivity Mapping Based on Remote Sensing in High-Latitude Regions: A Case Study on the Narsaq Region of Greenland. Minerals. 12, 692.
Helba, H., Trumbull, R., Morteani, G., Khalil, S., Arslan, A., 1997. Geochemical and petrographic studies of Ta mineralization in the Nuweibi albite granite complex, Eastern Desert, Egypt. Miner. Deposita. 32, 164–179.
Hewson, R.D., Cudahy, T., Huntington, J., 2001. Geologic and alteration mapping at Mt Fitton, South Australia, using ASTER satellite-borne data. IGARSS 2001 Scanning the Present and Resolving the Future Proceedings in: IEEE 2001 International Geoscience and Remote Sensing Symposium (Cat No 01CH37217): IEEE; 2001. p. 724-6.
Hussein, A., Aly, M., El Ramly, M., 1982. A proposed new classification of the granites of Egypt. J. Volcanol. Geoth. Res. 14, 187–198.
Imran, M., Ahmad, S., Sattar, A., Tariq, A., 2022. Mapping sequences and mineral deposits in poorly exposed lithologies of inaccessible regions in Azad Jammu and Kashmir using SVM with ASTER satellite data. Arab. J. Geosci. 15, 1–13.
Khan, S.D., Mahmood, K., Casey, J.F., 2007. Mapping of Muslim Bagh ophiolite complex (Pakistan) using new remote sensing, and field data. J. Asian Earth Sci. 30, 333–343.
Köhler, M., Hanelli, D., Schaefer, S., Barth, A., Knobloch, A., Hielscher, P., et al., 2021. Lithium potential mapping using artificial neural networks: a case study from Central Portugal. Minerals. 11, 1046.
Kruse, F.A., Boardman, J.W., Huntington, J.F., 2003. Comparison of airborne hyperspectral data and EO-1 Hyperion for mineral mapping. IEEE Trans. Geosci. Remote Sens. 41, 1388–1400.
Kumar, C., Shetty, A., Raval, S., Sharma, R., Ray, P.C., 2015. Lithological discrimination and mapping using ASTER SWIR Data in the Udaipur area of Rajasthan, India. Procedia Earth Planet. Sci. 11, 180–188.
Kumar, C., Chatterjee, S., Oommen, T., Guha, A., 2020. Automated lithological mapping by integrating spectral enhancement techniques and machine learning algorithms using AVIRIS-NG hyperspectral data in Gold-bearing granite-greenstone rocks in Hutti, India. Int. J. Appl. Earth Obs. Geoinf. 86, 102006.
Latifovic, R., Pouliot, D., Campbell, J., 2018. Assessment of convolution neural networks for surficial geology mapping in the South Rae geological region, Northwest Territories, Canada. Remote Sensng. 10, 307.
Liang, S., 2018. Comprehensive Remote Sensing. Elsevier.
Linnen, R.L., Van Lichtervelde, M., Černý, P., 2012. Granitic pegmatites as sources of strategic metals. Elements. 8, 275–280.
Madani, A., Emam, A., 2011. SWIR ASTER band ratios for lithological mapping and mineral exploration: a case study from El Hudi area, southeastern desert, Egypt. Arab. J. Geosci. 4, 45–52.
Maepa, F., Smith, R.S., Tessema, A., 2021. Support vector machine and artificial neural network modelling of orogenic gold prospectivity mapping in the Swayze greenstone belt, Ontario, Canada. Ore Geol. Rev. 130, 103968.
Mahdi, A.M., Eldosouky, A.M., El Khateeb, S.O., Youssef, A.M., Saad, A.A., 2022. Integration of remote sensing and geophysical data for the extraction of hydrothermal alteration zones and lineaments; Gabal Shilman basement area, Southeastern Desert, Egypt. J. Afr. Earth Sci. 194, 104640.
Maleki, M., Niroomand, S., Farahbakhsh, E., Modabberi, S., Tajeddin, H.A., 2021. Hydrothermal alteration and structural mapping of the Qolqoleh-Kasnazan shear zone in Iran using remote sensing data. Arab. J. Geosci. 14, 1–14.
Manap, H.S., San, B.T., 2022a. Data Integration for Lithological Mapping Using Machine Learning Algorithms. Earth Sci. Inf. 15, 1841–1859.
Manap, H.S., San, B.T., 2022b. Data Integration for Lithological Mapping Using Machine Learning Algorithms. Earth Sci. Inf. 1–19.
Mars, J.C., Rowan, L.C., 2006. Regional mapping of phyllic-and argillic-altered rocks in the Zagros magmatic arc, Iran, using Advanced Spaceborne Thermal Emission and Reflection Radiometer (ASTER) data and logical operator algorithms. Geosphere. 2, 161–186.
Mashkoor, R., Ahmadi, H., Rahmani, A.B., Pekkan, E., 2022. Detecting Li-Bearing Pegmatites Using Geospatial Technology: The Case of SW Konar Province, Eastern Afghanistan. Geocarto International.
Masoumi, F., Eslamkish, T., Abkar, A.A., Honarmand, M., Harris, J.R., 2017. Integration of spectral, thermal, and textural features of ASTER data using Random Forests classification for lithological mapping. J. Afr. Earth Sc. 129, 445–457.
Meneisy, M.Y., 1990. Volvanicity. In: Said, R. (Ed.), The Geology of Egypt. AA Balkema, Rotterdam, pp. 157–174.
Moghtaderi, A., Moore, F., Ranjbar, H., 2022. Testing ASTER and Sentinel-2 MSI Images to Discriminate Igneous and Metamorphic Rock Units in the Chadormalu Paleocrater, Central Iran. Can. J. Remote Sens. 48, 214–238.
Mohamed, M.-A.-M., 2013. Immiscibilty between silicate magma and aqueous fluids in Egyptian rare-metal granites: melt and fluid inclusions study. Arab. J. Geosci. 6, 4021–4033.
Mohamed, F.H., Abdalla, H.M., Helba, H., 1999. Chemistry of micas in rare-metal granitoids and associated rocks, Eastern Desert, Egypt. Int. Geol. Rev. 41, 932–948.
Mohammadpour, M., Bahroudi, A., Abedi, M., 2020. Automatic lineament extraction method in mineral exploration using CANNY algorithm and Hough transform. Geotectonics. 54, 366–382.
Mondal, A., Kundu, S., Chandniha, S.K., Shukla, R., Mishra, P., 2012. Comparison of support vector machine and maximum likelihood classification technique using satellite imagery. Int. J. Remote Sens. GIS. 1, 116–123.

Moussa, H.E., Asimow, P.D., Azer, M.K., Abou El Maaty, M.A., Akarish, A.I., Yanni, N.N., et al., 2021. Magmatic and hydrothermal evolution of highly-fractionated rare-metal granites at Gabal Nuweibi, Eastern Desert, Egypt. Lithos 400, 106405.
Naim, G.M., EI Miligy, A.T., Soliman, K.H., 1996. Tanatalum-Niobium_Tin mineralization in CenteralEasten Desert, Egypt. Proc Geol Surv Egypt Cent Conf, pp 599-622.
Nair, A., Mathew, G., 2012. Lithological discrimination of the Phenaimata felsic–mafic complex, Gujarat, India, using the Advanced Spaceborne Thermal Emission and Reflection Radiometer (ASTER). Int. J. Remote Sens. 33, 198–219.
Neto, A.C.B., Pereira, V.P., Ronchi, L.H., de Lima, E.F., Frantz, J.C., 2009. The world-class Sn, Nb, Ta, F (Y, REE, Li) deposit and the massive cryolite associated with the albite-enriched facies of the Madeira A-type granite, Pitinga mining district, Amazonas State, Brazil. Can. Mineral. 47, 1329–1357.
Ninomiya, Y., 2003. A stabilized vegetation index and several mineralogic indices defined for ASTER VNIR and SWIR data. In: IGARSS 2003 2003 IEEE International Geoscience and Remote Sensing Symposium Proceedings (IEEE Cat No 03CH37477). IEEE, pp. 1552–1554.
Ninomiya, Y., 2004. Lithologic mapping with multispectral ASTER TIR and SWIR data. Sensors, Systems, and Next-Generation Satellites VII. SPIE, pp. 180–190.
Ninomiya, Y., Fu, B., Cudahy, T.J., 2005. Detecting lithology with Advanced Spaceborne Thermal Emission and Reflection Radiometer (ASTER) multispectral thermal infrared "radiance-at-sensor" data. Remote Sens. Environ. 99, 127–139.
Ninomiya, Y., Fu, B., Cudahy, T.J., 2006. Corrigendum to "Detecting lithology with Advanced Spaceborne Thermal Emission and Reflection Radiometer (ASTER) multispectral thermal infrared "radiance-at-sensor" data"[Remote Sensing of Environment 99 (1–2): 127–139 (2005), ASTER special issue]. Remote Sens. Environ. 4, 567.
Okada, K., Ishii, M., 1993. Mineral and lithological mapping using thermal infrared remotely sensed data from ASTER simulator. in: Proceedings of IGARSS'93-IEEE International Geoscience and Remote Sensing Symposium: IEEE. p. 126-8.
Oommen, T., Misra, D., Twarakavi, N.K., Prakash, A., Sahoo, B., Bandopadhyay, S., 2008. An objective analysis of support vector machine based classification for remote sensing. Math. Geosci. 40, 409–424.
Otukei, J.R., Blaschke, T., 2010. Land cover change assessment using decision trees, support vector machines and maximum likelihood classification algorithms. Int. J. Appl. Earth Obs. Geoinf. 12, S27–S31.
Pearson, K., 1901. Principal components analysis. London, Edinburgh, Dublin Philos. Mag. J. Sci. 6, 559.
Perumal, K., Bhaskaran, R., 2010. Supervised classification performance of multispectral images. arXiv preprint arXiv:10024046. 2010.
Peyghambari, S., Zhang, Y., 2021. Hyperspectral remote sensing in lithological mapping, mineral exploration, and environmental geology: an updated review. J. Appl. Remote Sens. 15, 031501.
Pour, A.B., Hashim, M., 2011. Identification of hydrothermal alteration minerals for exploring of porphyry copper deposit using ASTER data, SE Iran. J. Asian Earth Sci. 42, 1309–1323.
Pour, A.B., Hashim, M., Park, Y., Hong, J.K., 2018. Mapping alteration mineral zones and lithological units in Antarctic regions using spectral bands of ASTER remote sensing data. Geocarto Int. 33, 1281–1306.
Pour, A.B., Hashim, M., Hong, J.K., Park, Y., 2019. Lithological and alteration mineral mapping in poorly exposed lithologies using Landsat-8 and ASTER satellite data: North-eastern Graham Land, Antarctic Peninsula. Ore Geol. Rev. 108, 112–133.
Qasim, M., Khan, S.D., Haider, R., 2022. Integration of multispectral and hyperspectral remote sensing data for lithological mapping in Zhob Ophiolite, Western Pakistan. Arab. J. Geosci. 15, 1–19.
Rajan Girija, R., Mayappan, S., 2019. Mapping of mineral resources and lithological units: A review of remote sensing techniques. Int. J. Image Data Fusion. 10, 79–106.
Ray, S., 2019. EXPLORING MACHINE LEARNING CLASSIFICATION ALGORITHMS FOR CROP CLASSIFICATION USING SENTINEL 2 DATA. Int. Arch. Photogram., Remote Sens. Spatial Inf. Sci.
Riad, A., 1979. Geology and petrology on some apogranite occurrence, Nuweibi area, Eastern Desert, Egypt. Al-Azhar University, Cairo, Egypt, p. 117. Master thesis.
Rodriguez-Galiano, V., Sanchez-Castillo, M., Chica-Olmo, M., Chica-Rivas, M., 2015. Machine learning predictive models for mineral prospectivity: An evaluation of neural networks, random forest, regression trees and support vector machines. Ore Geol. Rev. 71, 804–818.
Rokos, D., Argialas, D., Mavrantza, R., St-Seymour, K., Vamvoukakis, C., Kouli, M., et al., 2000. Structural analysis for gold mineralization using remote sensing and geochemical techniques in a GIS environment: island of Lesvos, Hellas. Natural Resour. Res. 9, 277–293.
Rowan, L.C., Mars, J.C., 2003. Lithologic mapping in the Mountain Pass, California area using advanced spaceborne thermal emission and reflection radiometer (ASTER) data. Remote Sens. Environ. 84, 350–366.
Rowan, L.C., Mars, J.C., Simpson, C.J., 2005. Lithologic mapping of the Mordor, NT, Australia ultramafic complex by using the Advanced Spaceborne Thermal Emission and Reflection Radiometer (ASTER). Remote Sens. Environ. 99, 105–126.
Sabet, A., LM B, AM R, LK A. Geologic structure and laws of localization of tantalum mineralization at the Nuweibi deposit. ANN GEOL SURV EGYPT; EGY; DA 1976; VOL 6; PP 119-156; HT 2; BIBL 8 REF; 8 ILL; 39 ANAL. 1976a.
Sabet A, LM B, LM B, MG M. Rare metal apogranites in Um Naggat massif. EgyptGeolSurv,Ann6,191–200. 1976b.
Sabet, A., Tsogoev, V., Shibanin, S., El-Kadi, M., Awad, S., 1976. The placer deposits of Igla, Abu Dabab and Nuweibi. Ann. Geol. Surv. Egypt. 6, 169–180.
Sabine C. Remote sensing strategies for mineral exploration. Remote Sensing for the Earth Sciences–Manuel of Remote Sensing. 1999:375-447.
Sabins, F.F., 2007. Remote sensing: principles and applications. Waveland Press.
Sabins, J., Floyd, F., 1986. Remote sensing: principles and interpretation. Chevron Oil Field Research Co.
Salehi, S., Mielke, C., Brogaard Pedersen, C., Dalsenni, O.S., 2019. Comparison of ASTER and Sentinel-2 spaceborne datasets for geological mapping: a case study from North-East Greenland. Geol. Surv. Denmark Greenland Bull. 43.
Sang, X., Xue, L., Ran, X., Li, X., Liu, J., Liu, Z., 2020. Intelligent high-resolution geological mapping based on SLIC-CNN. ISPRS Int. J. Geo-Inf. 9, 99.
Santos, D., Cardoso-Fernandes, J., Lima, A., Müller, A., Brönner, M., Teodoro, A.C., 2022. Spectral Analysis to Improve Inputs to Random Forest and other Boosted Ensemble Tree-Based Algorithms for Detecting NYF Pegmatites in Tysfjord, Norway. Remote Sens. 14, 3532.
Serbouti, I., Raji, M., Hakdaoui, M., Pradhan, B., Lee, C.-W., Alamri, A.M., 2021. Pixel and Object-Based Machine Learning Classification Schemes for Lithological Mapping Enhancement of Semi-Arid Regions Using Sentinel-2A Imagery: A Case Study of the Southern Moroccan Meseta. IEEE Access 9, 119262–119278.
Shabankareh, M., Hezarkhani, A., 2017. Application of support vector machines for copper potential mapping in Kerman region, Iran. J. Afr. Earth Sci. 128, 116–126.
Shebl, A., Abdellatif, M., Elkhateeb, S.O., Csámer, Á., 2021a. Multisource data analysis for gold potentiality mapping of Atalla area and its environs, Central Eastern Desert, Egypt. Minerals 11, 641.
Shebl, A., Csámer, Á., 2021b. Reappraisal of DEMs, Radar and optical datasets in lineaments extraction with emphasis on the spatial context. Remote Sens. Appl.: Soc. Environ. 24, 100617.
Shebl, A., Csámer, Á., 2021c. Stacked vector multi-source lithologic classification utilizing Machine Learning Algorithms: Data potentiality and dimensionality monitoring. Remote Sens. Appl.: Soc. Environ. 24, 100643.
Shebl, A., Abdellatif, M., Hissen, M., Abdelaziz, M.I., Csámer, Á., 2021b. Lithological mapping enhancement by integrating Sentinel 2 and gamma-ray data utilizing support vector machine: A case study from Egypt. Int. J. Appl. Earth Obs. Geoinf. 105, 102619.
Shebl, A., Abdelaziz, M.I., Ghazala, H., Araffa, S.A.S., Abdellatif, M., Csámer, Á., 2022. Multi-criteria ground water potentiality mapping utilizing remote sensing and geophysical data: A case study within Sinai Peninsula, Egypt. Egypt. J. Remote Sens. Space Sci. 25, 765–778.
Shebl, A., Csámer, Á., 2021. Lithological, structural and hydrothermal alteration mapping utilizing remote sensing datasets: a case study around Um Salim area, Egypt. IOP Conference Series: Earth and Environmental Science: IOP Publishing. p. 012032.
Sheikhrahimi, A., Pour, A.B., Pradhan, B., Zoheir, B., 2019. Mapping hydrothermal alteration zones and lineaments associated with orogenic gold mineralization using ASTER data: A case study from the Sanandaj-Sirjan Zone, Iran. Adv. Space Res. 63, 3315–3332.
Shirazy, A., Shirazi, A., Heidarlaki, S., Ziaii, M., 2018. Exploratory Remote Sensing Studies to Determine the Mineralization Zones around the Zarshuran Gold Mine. Int. J. Sci. Eng. Appl. 7, 274–279.
Shirmard, H., Farahbakhsh, E., Heidari, E., Beiranvand Pour, A., Pradhan, B., Müller, D., et al., 2022a. A Comparative Study of Convolutional Neural Networks and Conventional Machine Learning Models for Lithological Mapping Using Remote Sensing Data. Remote Sens. 14, 819.
Shirmard, H., Farahbakhsh, E., Müller, R.D., Chandra, R., 2022b. A review of machine learning in processing remote sensing data for mineral exploration. Remote Sens. Environ. 268, 112750.
Stern, R., 1979. Late Precambrian crustal environments as reconstructed from relict igneous minerals, Central Eastern Desert of Egypt. Ann. Geol. Surv. Egypt 9, 9–13.
Stern, R.J., 1981. Petrogenesis and tectonic setting of Late Precambrian ensimatic volcanic rocks, Central Eastern Desert of Egypt. Precambr. Res. 16, 195–230.
Stern, R.J., 2018. Neoproterozoic formation and evolution of Eastern Desert continental crust–The importance of the infrastructure-superstructure transition. J. Afr. Earth Sc. 146, 15–27.
Tangestani, M.H., Shayeganpour, S., 2020. Mapping a lithologically complex terrain using Sentinel-2A data: a case study of Suriyan area, southwestern Iran. Int. J. Remote Sens. 41, 3558–3574.
Tompolidi, A.-M., Sykioti, O., Koutroumbas, K., Parcharidis, I., 2020. Spectral unmixing for mapping a hydrothermal field in a volcanic environment applied on ASTER, Landsat-8/OLI, and Sentinel-2 MSI Satellite Multispectral Data: The Nisyros (Greece) case study. Remote Sens. 12, 4180.
Tripathi, M.K., Govil, H., Bhaumik, P., 2022. Implications and interrelations of litho-boundaries and vicinity of lineaments for hydrothermal alteration zones under remote sensing and GIS environment. Adv. Space Res.
Van der Meer, F., Van der Werff, H., Van Ruitenbeek, F., 2014. Potential of ESA's Sentinel-2 for geological applications. Remote Sens. Environ. 148, 124–133.
Vapnik, V.N., 1995. The nature of statistical learning Theory. Springer science & business media.
Varouchakis, E.A., Kamińska-Chuchmała, A., Kowalik, G., Spanoudaki, K., Graña, M., 2021. Combining geostatistics and remote sensing data to improve spatiotemporal analysis of precipitation. Sensors. 21, 3132.
Volesky, J.C., Stern, R.J., Johnson, P.R., 2003. Geological control of massive sulfide mineralization in the Neoproterozoic Wadi Bidah shear zone, southwestern Saudi Arabia, inferences from orbital remote sensing and field studies. Precambr. Res. 123, 235–247.
Wambo, J.D.T., Pour, A.B., Ganno, S., Asimow, P.D., Zoheir, B., dos Reis, S.R., et al., 2020. Identifying high potential zones of gold mineralization in a sub-tropical region using Landsat-8 and ASTER remote sensing data: a case study of the Ngoura-Colomines goldfield, eastern Cameroon. Ore Geol. Rev. 122, 103530.

Wu, G., Chen, G., Cheng, Q., Zhang, Z., Yang, J., 2021. Unsupervised machine learning for lithological mapping using geochemical data in covered areas of Jining, China. Natural Resour. Res. 30, 1053–1068.

Xi, Y., Mohamed Taha, A.M., Hu, A., Liu, X., 2022. Accuracy comparison of various remote sensing data in lithological classification based on random forest algorithm. Geocarto Int. 1–29.

Xiang, J., Xiao, K., Carranza, E.J.M., Chen, J., Li, S., 2020. 3D mineral prospectivity mapping with random forests: A case study of Tongling, Anhui, China. Natural Resour. Res. 29, 395–414.

Yajima, T., Yamaguchi, Y., 2013. Geological mapping of the Francistown area in northeastern Botswana by surface temperature and spectral emissivity information derived from Advanced Spaceborne Thermal Emission and Reflection Radiometer (ASTER) thermal infrared data. Ore Geol. Rev. 53, 134–144.

Yamaguchi, Y., Naito, C., 2003. Spectral indices for lithologic discrimination and mapping by using the ASTER SWIR bands. Int. J. Remote Sens. 24, 4311–4323.

Yamaguchi, Y., Kahle, A.B., Tsu, H., Kawakami, T., Pniel, M., 1998. Overview of advanced spaceborne thermal emission and reflection radiometer (ASTER). IEEE Trans. Geosci. Remote Sens. 36, 1062–1071.

Yang, J., Cheng, Q., 2015. A comparative study of independent component analysis with principal component analysis in geological objects identification, Part I: Simulations. J. Geochem. Explor. 149, 127–135.

Youssef, A.M., Pradhan, B., Dikshit, A., Mahdi, A.M., 2022. Comparative study of convolutional neural network (CNN) and support vector machine (SVM) for flood susceptibility mapping: a case study at Ras Gharib, Red Sea, Egypt. Geocarto Int. 1–28.

Yu, L., Porwal, A., Holden, E.-J., Dentith, M.C., 2012. Towards automatic lithological classification from remote sensing data using support vector machines. Comput. Geosci. 45, 229–239.

Zoheir, B., Lehmann, B., Emam, A., Radwan, A., Zhang, R., Bain, W.M., et al., 2020. Extreme fractionation and magmatic–hydrothermal transition in the formation of the Abu Dabbab rare-metal granite, Eastern Desert. Egypt. Lithos. 352, 105329.